

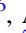


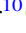


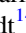









NuSTAR Survey of Obscured Swift/BAT-selected Active Galactic Nuclei. II. Median High-energy Cutoff in Seyfert II Hard X-Ray Spectra

M. Balokovic^{1,2,3,4} , F. A. Harrison⁵ , G. Madejski⁶ , A. Comastri⁷ , C. Ricci^{8,9} , A. Annuniaro¹⁰ , D. R. Ballantyne¹¹ , P. Boorman^{12,13} , W. N. Brandt^{14,15,16} , M. Brightman⁵ , P. Gandhi¹² , N. Kamraj⁵ , M. J. Koss¹⁷ , S. Marchesi^{7,18} ,

A. Marinucci¹⁹ , A. Masini²⁰ , G. Matt²¹ , D. Stern²² , and C. M. Urry¹ 

¹ Yale Center for Astronomy & Astrophysics, 52 Hillhouse Avenue, New Haven, CT 06511, USA; mislav.balokovic@yale.edu

² Department of Physics, Yale University, P.O. Box 208120, New Haven, CT 06520, USA

³ Center for Astrophysics | Harvard & Smithsonian, 60 Garden Street, Cambridge, MA 02138, USA

⁴ Black Hole Initiative at Harvard University, 20 Garden Street, Cambridge, MA 02138, USA

⁵ Cahill Center for Astronomy and Astrophysics, California Institute of Technology, 1200 East California Boulevard, Pasadena, CA 91125, USA

⁶ Kavli Institute for Particle Astrophysics and Cosmology, SLAC National Accelerator Laboratory, Stanford University, Stanford, CA 94305, USA

⁷ INAF—OAS Osservatorio di Astrofisica e Scienza dello Spazio di Bologna, Via Gobetti 93/3, I-40129 Bologna, Italy

⁸ Núcleo de Astronomía, Facultad de Ingeniería y Ciencias, Universidad Diego Portales, Av. Ejército Libertador 441, Santiago, Chile

⁹ Kavli Institute for Astronomy and Astrophysics, Peking University, Beijing 100871, People's Republic of China

¹⁰ Department of Applied Physics, Faculty of Science and Technology, Universiti Kebangsaan Malaysia, 43600 Bangi, Selangor, Malaysia

¹¹ Georgia Institute of Technology, 837 State Street, Atlanta, GA 30332, USA

¹² Department of Physics and Astronomy, University of Southampton, Southampton SO17 1BJ, UK

¹³ Astronomical Institute, Academy of Sciences, Boční II 1401, CZ-14131 Prague, Czech Republic

¹⁴ Department of Astronomy and Astrophysics, The Pennsylvania State University, University Park, PA 16802, USA

¹⁵ Institute for Gravitation and the Cosmos, The Pennsylvania State University, University Park, PA 16802, USA

¹⁶ Department of Physics, 104 Davey Laboratory, The Pennsylvania State University, University Park, PA 16802, USA

¹⁷ Eureka Scientific Inc., 2452 Delmer St., Suite 100, Oakland, CA 94602, USA

¹⁸ Department of Physics and Astronomy, Clemson University, Kinard Lab of Physics, Clemson, SC 29634, USA

¹⁹ Agenzia Spaziale Italiana (ASI)—Unità di Ricerca Scientifica, Via del Politecnico snc, I-00133 Roma, Italy

²⁰ Scuola Internazionale Superiore di Studi Avanzati, Via Bonomea 265, I-34136 Trieste, Italy

²¹ Università degli Studi Roma Tre, Via della Vasca Navale 84, I-00146 Roma, Italy

²² Jet Propulsion Laboratory, California Institute of Technology, Pasadena, CA 91109, USA

Received 2020 February 13; revised 2020 October 2; accepted 2020 October 19; published 2020 December 10

Abstract

Broadband X-ray spectroscopy of the X-ray emission produced in the coronae of active galactic nuclei (AGNs) can provide important insights into the physical conditions very close to their central supermassive black holes. The temperature of the Comptonizing plasma that forms the corona is manifested through a high-energy cutoff that has been difficult to directly constrain even in the brightest AGN because it requires high-quality data at energies above 10 keV. In this paper we present a large collection of coronal cutoff constraints for obscured AGNs based on a sample of 130 AGNs selected in the hard X-ray band with Swift/BAT and observed nearly simultaneously with NuSTAR and Swift/XRT. We find that under a reasonable set of assumptions regarding partial constraints the median cutoff is well constrained to 290 ± 20 keV, where the uncertainty is statistical and given at the 68% confidence level. We investigate the sensitivity of this result to our assumptions and find that consideration of various known systematic uncertainties robustly places the median cutoff between 240 and 340 keV. The central 68% of the intrinsic cutoff distribution is found to be between about 140 and 500 keV, with estimated uncertainties of 20 and 100 keV, respectively. In comparison with the literature, we find no clear evidence that the cutoffs in obscured and unobscured AGNs are substantially different. Our analysis highlights the importance of carefully considering partial and potentially degenerate constraints on the coronal high-energy cutoff in AGNs.

Unified Astronomy Thesaurus concepts: Active galactic nuclei (16); X-ray active galactic nuclei (2035); Seyfert galaxies (1447); High energy astrophysics (739); X-ray surveys (1824)

1. Introduction

The X-ray continuum emission in active galactic nuclei (AGNs) is thought to be produced in a region filled with a hot plasma—called the *corona*—which up-scatters optical and UV photons into the X-ray band through inverse Compton scattering (e.g., Vaiana & Rosner 1978; Haardt & Maraschi 1991; Merloni & Fabian 2003). Studies of the black hole mass dependence of AGN X-ray variability (e.g., Axelsson et al. 2013; McHardy 2013; Ludlam et al. 2015), reverberation of X-ray radiation reprocessed by the accretion disk (e.g., De Marco et al. 2013; Uttley et al. 2014; Kara et al. 2016), and quasar microlensing (e.g., Mosquera et al. 2013; Chartas et al. 2016; Guerras et al. 2017) all suggest that the AGN X-ray source is small in size and located close to the central

supermassive black hole (SMBH) and accretion disk, with a typical size scale of 2–20 gravitational radii of the black hole.

Broadband X-ray spectroscopy of the X-ray emission produced in the Comptonizing plasma can provide important insights into the principal properties of the corona, such as its temperature (kT_e) and optical depth (τ_e), and ultimately its geometry. The high-energy cutoff (E_{cut}) is a parameter of the commonly used approximation to the coronal continuum (e.g., Rothschild et al. 1983; Gondek et al. 1996; Dadina 2008): the power law with an exponential cutoff, $\propto E^{-\Gamma} e^{-E/E_{\text{cut}}}$, where E is photon energy and Γ is the photon index. Spectral parameters of this phenomenological model correspond to the physical parameters of the corona (e.g., Poutanen & Svensson 1996; Petrucci et al. 2001; Fabian et al. 2015), and E_{cut} is a proxy for

the coronal temperature (Middei et al. 2019). However, it has been difficult to constrain it observationally even in the brightest AGN, since it additionally requires high-quality data above 10 keV. As a result, our knowledge of the physical properties of the corona remains limited.

Many previous studies of E_{cut} in nearby AGNs implied that its typical value is of the order of 100 keV, starting already with early studies using hard X-ray data from HEAO-1 and CGRO/OSSE (e.g., Rothschild et al. 1983; Gondek et al. 1996; Zdziarski et al. 2000). Coronal cutoffs in unobscured AGNs have been the topic of many observational studies over the past decade (e.g., Panessa et al. 2008; Ricci et al. 2011; Malizia et al. 2014). The field has gained new momentum since the launch of NuSTAR (Harrison et al. 2013), whose focusing ability boosted data quality in the hard X-ray band (3–79 keV) far above that of nonfocusing instruments. Summaries of early NuSTAR measurements for individual bright AGNs can be found in Fabian et al. (2015) and Tortosa et al. (2018b). Kamraj et al. (2018) and Molina et al. (2019) recently presented E_{cut} constraints for larger samples of unobscured AGNs observed with NuSTAR selected using Swift/BAT and INTEGRAL, respectively.

Constraints on E_{cut} in obscured AGNs are scarce in the literature despite the prevalence of such AGNs in the local universe, and especially at high redshift (e.g., Buchner et al. 2015; Hickox & Alexander 2018; Ananna et al. 2019). Their collective contribution dominates the cosmic X-ray background (CXB) around its broad peak at 30 keV. The median E_{cut} is an important ingredient of CXB synthesis models (e.g., Comastri et al. 1995; Gilli et al. 2007; Akylas et al. 2012) that enable us to distinguish different AGN populations and probe their evolution. In particular, at $\gtrsim 100$ keV contributions from unobscured and obscured Seyfert galaxies become comparable to those of blazars (Ajello et al. 2009; Draper & Ballantyne 2009), with the exact proportions depending directly on the assumed typical E_{cut} . Through CXB modeling, better constraints on E_{cut} also help to evaluate the importance of relativistic light bending to X-ray spectra of AGNs (Gandhi et al. 2007) and the prevalence of highly spinning SMBHs (Vasudevan et al. 2016).

E_{cut} has been well constrained using NuSTAR data in only a handful of obscured AGNs thus far: NGC 4945 (Puccetti et al. 2014), MCG –05-23-016 (Baloković et al. 2015), ESO 103-G035 (Buisson et al. 2018), Mrk 1498 (Ursini et al. 2018a), NGC 262, NGC 2992, NGC 7172 (Rani et al. 2019), NGC 2110, and NGC 4388 (Ursini et al. 2019). Additionally, lower limits on E_{cut} based on NuSTAR data have been derived for obscured sources NGC 5506 (Matt et al. 2015), Cyg A (Reynolds et al. 2015), Cen A (Fürst et al. 2016), PKS 2331–240, and PKS 2356–61 (Ursini et al. 2018a). Some constraints based on lower-quality data from nonfocusing hard X-ray instruments exist in the literature, e.g., from BeppoSAX (Dadina 2007), Suzaku (Tazaki et al. 2011), RXTE (Rivers et al. 2011), INTEGRAL (de Rosa et al. 2012), Swift/BAT (Vasudevan et al. 2013; Ricci et al. 2017), or a combination thereof (Molina et al. 2013).

In this paper we present the first large sample of coronal cutoff constraints for obscured AGNs with data quality that exceeds that of nonfocusing telescopes in the hard X-ray band. The work presented here is based on a survey of the nearby obscured AGN population with NuSTAR and Swift, sampling over 130 bright AGNs selected from the Swift/BAT all-sky survey (M. Baloković et al. 2020, in preparation, hereafter

Paper I; see also Baloković 2017). While studies of larger samples with more limited data and individual AGNs with higher-quality data exist in the literature (e.g., Ricci et al. 2017; Zoghbi et al. 2017, respectively), our study represents an unprecedented combination of excellent data quality and large sample size. This provides a unique opportunity to characterize the average properties of the corona in the highly obscured population and enables comparative studies of coronae in different kinds of AGNs.

2. Data Selection and Analysis

2.1. Short Summary of Paper I

Data selection, processing, and the bulk of spectral analysis are described in detail in Paper I; here we only provide a brief summary. The sample used in both works is based on the Swift/BAT AGN catalog compiled using 70 months of data collection (Baumgartner et al. 2013), which selects AGNs bright in the hard X-ray band (14–195 keV), with high completeness for obscured AGNs up to high obscuring columns (Ricci et al. 2017). We focus on a group of AGNs optically classified as types 2, 1.9, and 1.8, including some narrow-line LINERs, regardless of their infrared or polarized spectra. Both in Paper I and here, we refer to this group as type II Seyfert galaxies (Sy II), denoted with roman numerals to emphasize the difference with the optical classes differentiated by arabic numerals. The optical class was taken from the Swift/BAT catalog supplemented by the updated spectroscopy and more uniform classification (following Osterbrock 1981) provided by the BAT AGN Spectroscopic Survey (BASS;²³ Koss et al. 2017).

For the majority of our sample, the observed X-ray spectrum was built from a single NuSTAR observation (median exposure 21 ks), a contemporaneous Swift/XRT observation (median exposure 6 ks), and a time-averaged Swift/BAT spectrum (effective exposure $\simeq 8$ Ms). Any targets for which NuSTAR or Swift data were co-added or excluded are marked with a note in Table 1. The median source count rate is $0.1 \text{ counts s}^{-1}$ per NuSTAR module (FPM), compared to $2 \times 10^{-5} \text{ counts s}^{-1}$ for Swift/BAT. For grouping of the NuSTAR and Swift/XRT spectra into energy bins, we used a custom procedure described by Baloković (2017) that results in the total number of bins proportional to data quality and a roughly constant signal-to-noise ratio (S/N) per bin, with a floor at $S/N > 3$. In spectral fitting, we used Swift/BAT data simultaneously with NuSTAR and Swift/XRT data except in several cases of substantially different flux, as noted in Table 1.

The key spectral analysis presented in Paper I is based on fitting a simple phenomenological spectral model for obscured AGNs in *Xspec* (Arnaud 1996). The data selection briefly described above and the spectral analysis define our *uniform sample*. Numbering 130 AGNs, it covers more than 50% of the parent Swift/BAT 70-month Sy II sample and is statistically consistent with a random draw from that sample. It excludes AGNs with updated optical classification inconsistent with Sy II and AGNs with complex X-ray spectra inconsistent with our chosen X-ray spectral model.

The model we employ is used ubiquitously in the literature and consists of components typically observed in X-ray spectra of obscured AGNs: an intrinsic cutoff power-law continuum,

²³ <https://www.bass-survey.com/>

Table 1
Constraints on Parameters of the Hard X-Ray Continuum Model

Target Name	χ^2/ν	$P_{\text{null}}/\%$	Γ	$E_{\text{cut}}/\text{keV}$	τ_e^a	Notes ^b
NGC 262	503.0/464	10	1.66 ± 0.04	170_{-30}^{+40}	2.1	RL, 1.9
ESO 195-IG021	224.7/249	86	1.88 ± 0.09	>230	1.0	...
NGC 454 E	56.2/79	98	$1.6_{-0.5}^{+0.3}$	>50	5.4	...
NGC 513	126.5/140	79	$1.77_{-0.15}^{+0.03}$	>230	1.2	...
NGC 612	102.1/126	94	$1.47_{-0.09}^{+0.25}$	170_{-50}^{+u}	2.8	RL
2MASX J0140	195.1/235	97	1.59 ± 0.09	70_{-20}^{+40}	4.4	...
MCG -01-05-047	98.9/114	84	1.7 ± 0.2	200_{-100}^{+u}	1.8	...
NGC 788	121.1/149	96	1.7 ± 0.2	200_{-100}^{+u}	1.4	...
ESO 416-G002	147.3/156	68	1.68 ± 0.03	>480	0.7	1.9
NGC 1052	179.9/211	94	1.36 ± 0.09	80_{-20}^{+40}	5.4	RL, 1.9
2MFGC 2280	24.9/37	94	1.4 ± 0.5	130_{-80}^{+u}	3.8	...
NGC 1194	163.8/175	72	1.5 ± 0.2	140_{-60}^{+100}	3.3	...
NGC 1229	112.8/100	18	$1.6_{-0.4}^{+0.1}$	>82.4	3.7	C
MCG +00-09-042	249.1/248	47	$2.07_{-0.10}^{+0.03}$	>190	0.9	...
NGC 1365	436.8/428	37	1.90 ± 0.08	290_{-100}^{+200}	0.8	...
2MASX J0356	177.9/155	10	$1.69_{-0.09}^{+0.04}$	>240	1.4	...
3C 105	90.1/92	54	1.8 ± 0.3	>70	3.5	C, RL
2MASX J0423	115.3/119	58	$1.4_{-0.4}^{+0.2}$	70_{-30}^{+40}	5.5	...
MCG +03-13-001	93.3/88	33	$1.9_{-0.4}^{+0.1}$	>60	3.4	C, 1.9
CGCG 420-015	267.9/244	14	1.8 ± 0.2	190_{-90}^{+u}	1.4	C
ESO 033-G002	379.5/428	96	2.20 ± 0.07	>460	0.4	...
LEDA 178130	374.5/384	63	$1.68_{-0.06}^{+0.08}$	350_{-150}^{+u}	0.9	...
2MASX J0508	352.7/321	11	1.71 ± 0.07	160_{-60}^{+200}	2.1	1.9
ESO 553-G043	314.1/327	69	1.71 ± 0.06	>190	1.8	...
NGC 2110	687.2/661	23	1.64 ± 0.02	300_{-30}^{+50}	1.1	A
ESO 005-G004	60.9/56	30	$1.83_{-0.05}^{+0.18}$	>140	2.1	B
Mrk 3	539.3/541	51	1.52 ± 0.08	150_{-30}^{+60}	2.8	1.9
ESO 121-IG028	156.3/186	94	$1.87_{-0.17}^{+0.09}$	>150	1.7	...
LEDA 549777	98.5/104	64	1.4 ± 0.1	>90	4.4	...
LEDA 511628	185.5/208	87	1.6 ± 0.1	90_{-30}^{+80}	3.4	...
MCG +06-16-028	101.8/91	20	$1.8_{-0.3}^{+0.1}$	>110	2.4	1.9
IRAS 07378-3136	226.2/229	54	1.3 ± 0.2	60_{-20}^{+40}	6.8	...
UGC 3995 A	167.9/188	85	1.5 ± 0.2	100_{-40}^{+110}	3.6	...
Mrk 1210	284.3/286	52	1.6 ± 0.1	90_{-20}^{+40}	3.6	1.9
MCG -01-22-006	350.3/367	73	1.4 ± 0.1	110_{-30}^{+60}	4.7	...
CGCG 150-014	105.3/104	44	$1.78_{-0.33}^{+0.05}$	>110	2.5	RL
MCG +11-11-032	60.9/64	59	$1.97_{-0.04}^{+0.16}$	>140	1.7	...
2MASX J0903	60.5/57	35	1.9 ± 0.2	>270	0.9	C
2MASX J0911	116.8/133	84	1.50 ± 0.09	70_{-20}^{+60}	4.9	...
IC 2461	243.3/247	56	1.8 ± 0.1	200_{-90}^{+u}	1.4	...
MCG -01-24-012	296.8/327	88	1.93 ± 0.09	110_{-30}^{+50}	2.2	...
2MASX J0923	82.0/85	57	1.1 ± 0.6	40_{-20}^{+90}	>7	...
NGC 2992	653.7/719	96	1.74 ± 0.02	>380	0.8	A, 1.9
MCG -05-23-016	811.4/780	21	1.93 ± 0.02	150 ± 10	1.6	A, 1.9
NGC 3079	91.7/102	76	1.1 ± 0.4	40_{-10}^{+20}	>7	...
ESO 263-G013	136.3/139	55	1.7 ± 0.2	>120	2.7	...
NGC 3281	176.1/199	88	$1.25_{-0.11}^{+0.09}$	70 ± 10	>7	...
MCG +12-10-067	130.3/138	67	$2.0_{-0.3}^{+0.1}$	>108.7	2.1	...
MCG +06-24-008	139.1/146	64	$1.60_{-0.08}^{+0.05}$	>170	2.3	...
UGC 5881	95.9/94	43	1.3 ± 0.3	80_{-30}^{+120}	5.8	...
NGC 3393	57.8/77	95	$1.8_{-0.3}^{+0.2}$	160_{-100}^{+u}	2.0	...
Mrk 417	219.0/218	47	1.51 ± 0.02	130_{-40}^{+120}	3.2	...
2MASX J1136	270.3/259	30	2.02 ± 0.03	>350	0.6	...
NGC 3822	96.8/114	88	1.7 ± 0.1	>70	3.8	...
B2 1204+34	177.5/207	93	1.70 ± 0.05	>280	1.1	RL
IRAS 12074-4619	169.0/180	71	$1.85_{-0.06}^{+0.03}$	>320	0.8	1.9
WAS 49	99.2/99	48	1.4 ± 0.3	60_{-20}^{+60}	6.2	...
NGC 4258	240.6/257	76	$1.82_{-0.12}^{+0.05}$	>180	1.5	1.9
NGC 4388	346.5/311	8	$1.64_{-0.06}^{+0.08}$	210_{-40}^{+120}	1.8	A, X
NGC 4395	276.3/305	88	1.54 ± 0.08	120_{-30}^{+50}	3.3	1.9

Table 1
(Continued)

Target Name	χ^2/ν	$P_{\text{null}} / \%$	Γ	$E_{\text{cut}}/\text{keV}$	τ_e^a	Notes ^b
NGC 4507	662.7/715	92	$1.41^{+0.09}_{-0.11}$	80^{+20}_{-10}	5.2	1.9
LEDA 170194	130.3/140	71	$1.79^{+0.04}_{-0.12}$	>230	1.1	...
NGC 4941	58.6/57	42	$1.5^{+0.3}_{-0.5}$	110^{+u}_{-60}	3.6	...
NGC 4939	132.4/135	55	1.8 ± 0.2	>140	2.1	...
NGC 4945	499.8/473	19	1.91 ± 0.03	>240	0.9	B
NGC 4992	283.1/248	6	1.2 ± 0.4	80^{+90}_{-30}	> 7	...
Mrk 248	141.3/166	92	1.6 ± 0.1	50^{+20}_{-10}	5.5	...
Cen A	727.2/698	22	1.765 ± 0.007	550^{+140}_{-90}	0.5	A, B, RL
ESO 509-IG066	199.2/224	88	1.5 ± 0.1	70^{+50}_{-20}	4.4	1.9
NGC 5252	299.7/292	36	1.67 ± 0.04	330^{+150}_{-100}	0.9	X
2MASX J1410	145.7/123	8	1.8 ± 0.2	>80	3.3	...
NGC 5506	197.9/181	18	1.79 ± 0.02	110 ± 10	2.7	A, 1.9
NGC 5643	125.8/115	23	1.9 ± 0.2	>130	2.0	C
NGC 5674	244.0/258	73	1.86 ± 0.09	210^{+u}_{-110}	1.1	...
Mrk 477	183.4/189	60	$1.6^{+0.2}_{-0.1}$	140^{+200}_{-60}	2.6	1.9
NGC 5728	271.4/270	46	$1.3^{+0.1}_{-0.2}$	80^{+30}_{-20}	6.9	1.9
IC 4518A	125.9/130	59	$1.8^{+0.2}_{-0.1}$	120^{+150}_{-50}	2.3	...
2MASX J1506	78.2/94	88	$1.71^{+0.06}_{-0.09}$	>140	2.4	...
NGC 5899	227.3/239	70	$1.96^{+0.08}_{-0.05}$	>340	0.6	...
MCG +11-19-006	85.2/72	14	$1.5^{+0.2}_{-0.4}$	>60	5.5	1.9
MCG -01-40-001	159.8/210	99	1.8 ± 0.1	260^{+u}_{-130}	1.0	1.9
NGC 5995	394.8/393	46	$2.02^{+0.05}_{-0.01}$	>340	0.6	1.9
MCG +14-08-004	92.0/99	68	1.7 ± 0.2	>120	2.6	...
Mrk 1498	325.3/307	23	$1.35^{+0.10}_{-0.05}$	60 ± 10	6.8	RL
IRAS 16288+3929	54.2/66	85	1.7 ± 0.3	130^{+u}_{-70}	2.7	...
ESO 137-G034	81.4/84	56	$1.81^{+0.05}_{-0.25}$	>160	1.8	...
LEDA 214543	294.4/340	96	1.83 ± 0.09	>170	1.6	...
NGC 6240	309.9/319	63	1.4 ± 0.2	90^{+70}_{-30}	4.6	1.9
NGC 6300	338.2/303	8	1.85 ± 0.06	210^{+100}_{-50}	1.1	A
MCG +07-37-031	203.9/192	26	1.66 ± 0.09	200^{+u}_{-90}	1.9	...
2MASX J1824	152.2/162	70	$1.8^{+0.1}_{-0.2}$	>110	2.5	1.9
IC 4709	212.5/218	59	1.8 ± 0.2	140^{+200}_{-60}	2.1	...
LEDA 3097193	376.4/392	70	1.78 ± 0.07	130^{+110}_{-40}	2.3	...
ESO 103-G035	327.9/349	78	1.78 ± 0.05	100^{+20}_{-10}	2.7	1.9
ESO 231-G026	186.1/234	99	$1.67^{+0.03}_{-0.11}$	>250	1.3	...
2MASX J1926	76.5/90	84	1.9 ± 0.2	150^{+u}_{-80}	1.8	...
2MASX J1947	245.0/252	61	1.8 ± 0.1	120^{+110}_{-40}	2.5	...
3C 403	168.0/180	73	1.5 ± 0.2	>110	3.6	RL
Cyg A	629.3/633	53	1.58 ± 0.08	130^{+70}_{-30}	2.9	B, RL
2MASX J2006	102.0/113	76	1.9 ± 0.2	>80	2.6	...
2MASX J2018	240.2/253	71	1.6 ± 0.2	170^{+u}_{-70}	2.4	...
2MASX J2021	134.1/133	46	1.7 ± 0.2	>90	3.1	...
NGC 6921	42.2/68	99	1.7 ± 0.2	190^{+u}_{-90}	1.7	C
MCG +04-48-002	70.2/74	60	1.7 ± 0.2	>150	2.3	C
IC 5063	291.5/287	42	$1.7^{+0.2}_{-0.1}$	220^{+u}_{-90}	1.3	RL
NGC 7130	82.1/72	20	$1.91^{+0.07}_{-0.30}$	>100	2.4	1.9
NGC 7172	774.5/769	44	1.88 ± 0.02	>670	0.4	A
MCG +06-49-019	59.3/60	50	$1.57^{+0.06}_{-0.08}$	>200.0	2.2	1.9
NGC 7319	95.7/93	40	$1.71^{+0.04}_{-0.18}$	>220	1.4	...
3C 452	357.1/418	99	1.3 ± 0.1	70^{+40}_{-20}	6.2	RL, 1.9
NGC 7582	294.4/298	55	1.7 ± 0.2	200^{+190}_{-80}	1.8	...
2MASX J2330	71.1/78	70	1.7 ± 0.3	>70	3.7	...
PKS 2331-240	304.6/278	13	1.80 ± 0.05	220^{+u}_{-110}	1.2	RL
PKS 2356-61	127.6/157	96	1.7 ± 0.2	160^{+u}_{-80}	2.1	RL

Notes.

^a Optical depth approximately calculated using Equation (3) and best-fit spectral parameters Γ and E_{cut} (or lower limit if best-fit value for the latter is undefined). Values greater than 3 are highlighted in bold font.

^b Notes: A = details discussed in the Appendix; B = Swift/BAT data excluded from spectral fitting; C = NuSTAR or Swift/XRT data co-added; X = Swift/XRT data not included; RL = radio-loud AGNs (see Section 4.2.3); 1.9 = optical type 1.9 according to Koss et al. (2017).

absorbed by a neutral column density, with reprocessing features represented by a `pexrav` (Magdziarz & Zdziarski 1995) continuum and a narrow Fe K α line at 6.4 keV in the rest frame, and a secondary power law (from extranuclear scattering on free electrons) emerging unabsorbed in the soft X-ray band. In `Xspec`, the model expression is

$$m = c_{\text{ins}} \times \text{phabs} \times (\text{zphabs} \times \text{cabs} \times \text{cutoffpl} + f_s \times \text{cutoffpl} + \text{zgauss} + \text{pexrav}),$$

where c_{ins} is an instrumental cross-normalization factor. We refer to this model as the *full model*. Its free spectral parameters are the photon index (Γ), line-of-sight column density (N_{H}), Compton hump normalization (R_{pex} , the absolute value of the negative R parameter in `pexrav`), Fe K α equivalent width ($\text{EW}_{\text{Fe K}\alpha}$), and relative normalization of the secondary power law (f_s). Paper I presents constraints on these phenomenological spectral parameters for all 130 AGNs in the *uniform sample* while keeping E_{cut} fixed at 300 keV.

2.2. Spectral Analysis with Free E_{cut}

The study presented here continues the analysis presented in Paper I by additionally letting the E_{cut} parameter be fitted instead of being fixed at 300 keV. This does not typically result in a significantly better fit to our data, but it does provide previously unavailable information on obscured AGN coronae. Data for three AGNs in our sample (Cen A, NGC 5506, and MCG -05-23-016) require a fitted E_{cut} in order to reach a statistically acceptable χ^2 according to our adopted null-probability (p_{null}) rejection threshold at 5%. Spectral models with free E_{cut} are therefore already discussed in Paper I for these targets. For the rest of the sample we simply include E_{cut} as an additional free parameter in order to test whether the data yield at least partial constraints on E_{cut} from spectral fitting. Since E_{cut} is an additional parameter in a model that already fits the data for all sources well, the resulting improvements in terms of χ^2 are not statistically significant in most cases. As expected, the obtained constraints are consistent with 300 keV in nearly all cases, although not always within the derived 68% confidence interval. Throughout this paper, as well as in Paper I, we define the single-parameter 68% confidence interval using a difference of $\Delta\chi^2 = 1$ with respect to the best fit while allowing the other parameters to freely vary in the fit.

Spectral analysis for the whole sample presented in Paper I resulted in constraints on E_{cut} for 114 AGNs in total. There is a clear difference in quality of constraints: some spectra yield the best-fit value, $E_{\text{cut}}^{\text{b.f.}}$, with both lower and upper limits of the 68% confidence interval ($E_{\text{cut}}^{\text{l.l.}}$ and $E_{\text{cut}}^{\text{u.l.}}$, respectively), while others yield only partial constraints. Examples of three constraint classes are shown in Figure 1. Out of 130 AGNs considered in Paper I, we find full constraints for 45, partial constraints for 69 (of which 50 yield only $E_{\text{cut}}^{\text{l.l.}}$, while for 19 we also find a $E_{\text{cut}}^{\text{b.f.}}$), and no constraints for 16. Although `Xspec` formally finds $E_{\text{cut}}^{\text{b.f.}}$ for more than 64 targets, in the remainder of such cases the difference in χ^2 from the best-fit value ($\Delta\chi^2$) for $E_{\text{cut}} > E_{\text{cut}}^{\text{b.f.}}$ is so small that we cannot consider $E_{\text{cut}}^{\text{b.f.}}$ reliably constrained.²⁴ Likewise, fits with $E_{\text{cut}}^{\text{u.l.}} > 500$ keV are

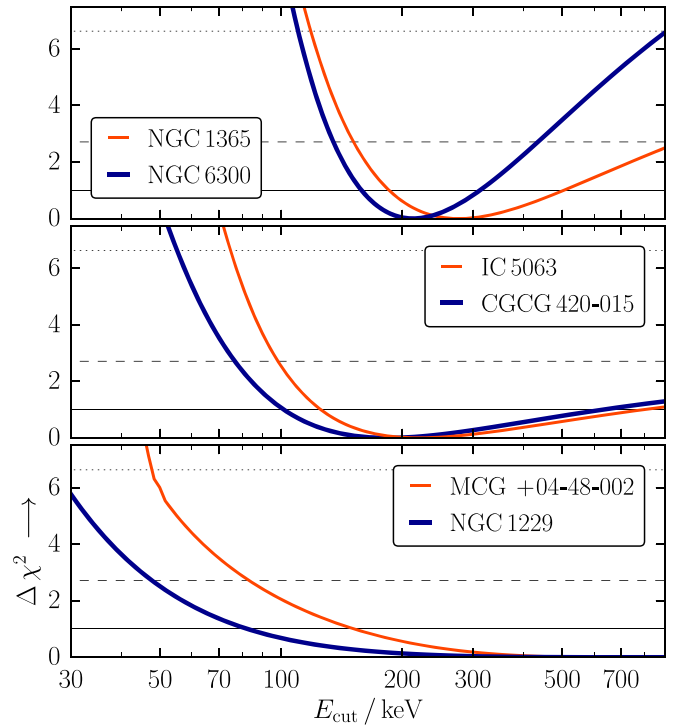


Figure 1. Representative examples of $\Delta\chi^2$ curves over the E_{cut} parameter space. Horizontal solid, dashed, and dotted lines mark the $\Delta\chi^2$ levels corresponding to 68%, 90%, and 99% confidence, respectively. All other spectral parameters are free to vary. In the top panel E_{cut} is fully constrained (yielding a best-fit value and two-sided uncertainty), in the middle panel it is partially constrained (lower limit and a weakly constrained best-fit value), and in the bottom panel examples provide only a lower limit.

unlikely to be reliable except in a few cases of high-quality data. We discard such $E_{\text{cut}}^{\text{b.f.}}$ and $E_{\text{cut}}^{\text{u.l.}}$ values on the basis of limited data quality. The statistics of constraints quoted above already include these quality-based cuts. The spectral fitting results described in this section are listed in Table 1.

2.3. Exclusion of Potentially Degenerate Constraints

Spectral parameters of the model defined in Section 2.1 are not fully independent, leading to degeneracy between fitted parameters that depends on both data quality and the spectral shape. The degeneracy between parameters Γ and E_{cut} is well known in the literature, as it also affects studies of E_{cut} in unobscured AGNs (e.g., Kamraj et al. 2018; Tortosa et al. 2018a; Molina et al. 2019). In Figure 2 we provide several examples. Unlike other pairs of parameters in our model, Γ and E_{cut} are always tightly correlated in the same direction, leading to a cumulative, systematic effect in studies of large samples. For obscured AGNs, this problem is exacerbated, as obscuration limits the energy range over which the coronal continuum is sampled directly.

In fitting spectra over a limited energy band, not all constraints on E_{cut} should be considered credible. Some very low best-fit values of E_{cut} are a simple consequence of a simultaneously low E_{cut} and Γ . Although the spectral shape formally fits the data very well, such combinations of Γ and E_{cut} do not correspond to a spectrum that could realistically be generated in the physical conditions expected in an AGN corona (see, e.g., Zdziarski & Lightman 1985; Stern et al. 1995; Poutanen & Svensson 1996). In order to avoid a possible bias from spurious low- E_{cut} and low- Γ fits, we devised a simple way

²⁴ In simulated data with the same spectral parameters and matching data quality, these values cannot be consistently recovered. Although $\Delta\chi^2 > 1$ (as in the examples shown in the middle panel of Figure 1) formally implies that $E_{\text{cut}}^{\text{u.l.}}$ can be defined, simulations we performed strongly suggest that our data cannot reliably constrain these values.

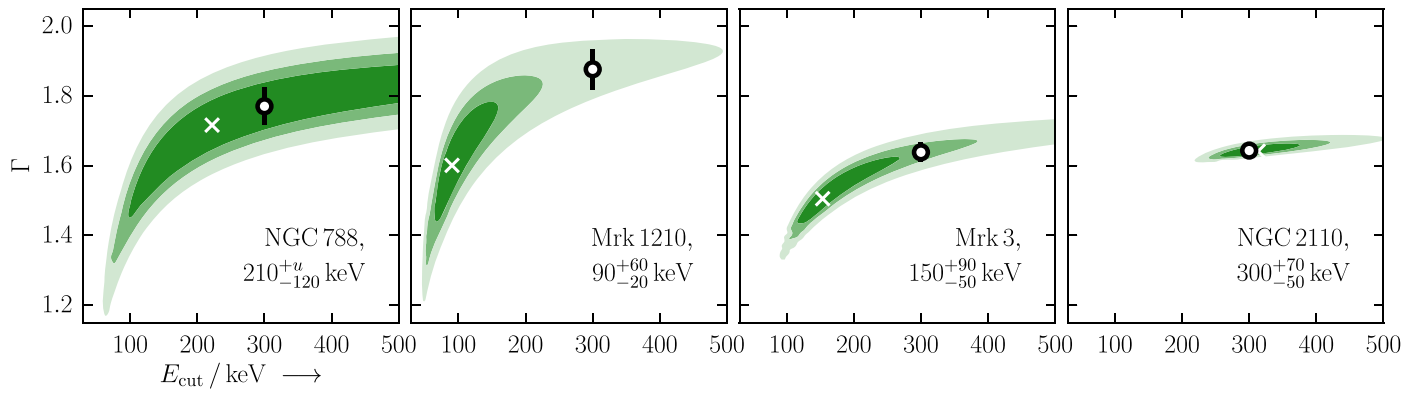


Figure 2. Three representative examples of the degeneracy between parameters Γ and E_{cut} shown as 1σ , 2σ , and 3σ contours (going from darker to lighter green) in the parameter space spanned by these two spectral parameters. In each panel, the best fit is marked with a white cross, and the open black circle with an error bar shows the best-fit Γ and its 1σ uncertainty with the assumption of $E_{\text{cut}} = 300$ keV (from a statistically acceptable model presented in Paper I). From left to right, the figure shows a progression from lowest to highest quality of E_{cut} constraint, with the second panel (Mrk 1210) showing an example of a result excluded to mitigate the parameter degeneracy (see Section 2.3).

to separate credible E_{cut} constraints from those potentially affected by the parameter degeneracy via a cut in implied electron scattering optical depth (τ_e), which can be approximated as a function of Γ and E_{cut} under reasonable assumptions.

For the conversion of phenomenological spectral parameters Γ and E_{cut} to basic physical parameters of the corona, kT_e and τ_e , we adopt the following approximations. First, $kT_e = E_{\text{cut}} / j(\tau_e)$, where

$$j(\tau_e) = \begin{cases} 2, & \text{if } \tau_e \leq 1, \\ \tau_e + 1, & \text{if } 1 < \tau_e < 2, \\ 3, & \text{if } \tau_e \geq 2. \end{cases} \quad (1)$$

We construct the continuous relation above based on two commonly assumed limiting cases for kT_e , $E_{\text{cut}}/2$ for $\tau_e \leq 1$ and $E_{\text{cut}}/3$ for $\tau_e \gg 1$ (e.g., Shapiro et al. 1976), noting that more realistic coronal models cover a wider range of scaling factors (Middei et al. 2019). kT_e , Γ , and τ_e are related via an approximate expression derived for a plane-parallel corona and formally valid for $\tau_e \gtrsim 1$ (Zdziarski 1985; Petrucci et al. 2001):

$$\Gamma = \sqrt{\frac{9}{4} + \frac{511 \text{ keV}}{kT_e \tau_e (1 + \tau_e/3)}} - \frac{1}{2}. \quad (2)$$

Inverting this relation, we compute τ_e from measured Γ and E_{cut} by iteratively solving the following equation:

$$\tau_e(1 + \tau_e/3)/j(\tau_e) = \frac{511 \text{ keV}/E_{\text{cut}}}{(\Gamma + 1/2)^2 - 9/4}. \quad (3)$$

Equation (3) defines a series of curves with constant τ_e in the plane spanned by parameters E_{cut} and Γ , as shown in Figure 3. For our fiducial analysis, we choose to separate credible E_{cut} constraints from the likely degenerate ones with a $\tau_e < 3$ cut. This cut should not be interpreted as a physical limit on the optical depth; rather, it is a practical way of excluding potentially degenerate constraints. While the exact value for the cut is arbitrary, we argue that one has to be made in order to avoid bias that may be purely due to the $E_{\text{cut}}-\Gamma$ degeneracy. This is examined in more detail in Section 4.

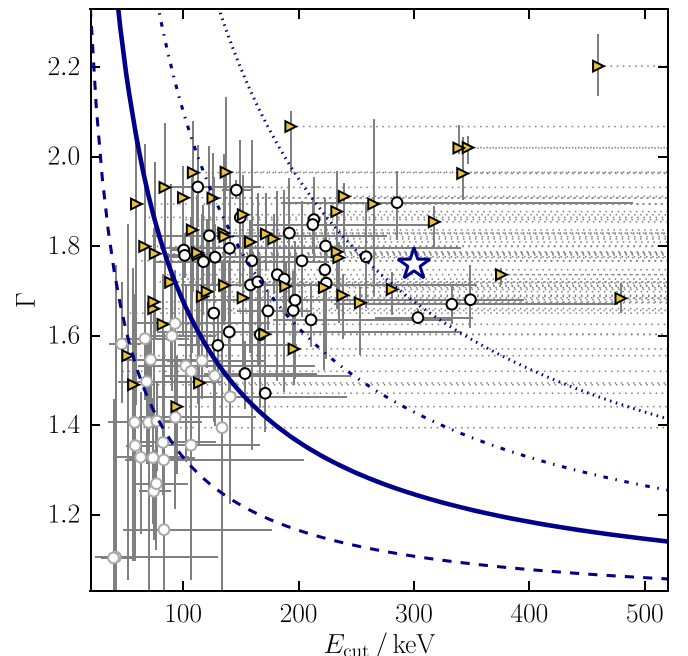


Figure 3. Distribution of spectral fitting results in the $E_{\text{cut}}-\Gamma$ plane. White-filled circles mark best-fit values where they could be obtained, while yellow-filled triangles mark lower limits on E_{cut} . Thin gray lines show individual error bars, with those that formally extend above 500 keV shown with dotted lines for clarity. The blue star marks the median Γ obtained with fixed $E_{\text{cut}} = 300$ keV in Paper I. The blue lines are defined by Equation (3) and mark $\tau_e = 1, 2, 3$, and 5 with dotted, dashed-dotted, solid, and dashed lines, respectively. We discard constraints with a best-fit value below the solid line in order to minimize bias due to the $E_{\text{cut}}-\Gamma$ degeneracy, which causes some fits to drift to extremely low values of both E_{cut} and Γ (see Figure 2).

3. Results

3.1. Summary of Individual Constraints

Our sample covers a factor of $\simeq 50$ in hard X-ray flux. NuSTAR exposures (3.7–57 ks) do not scale with the targets' flux, so the number of degrees of freedom (ν , a proxy of overall data quality) ranges between 30 and 770. Targets with $\nu \lesssim 60$ consistently do not provide any E_{cut} constraints. For $\nu \gtrsim 60$ the data typically provide lower limits on E_{cut} , and full constraints in some cases. Higher-quality data generally allow for stronger,

more stringent constraints with a range demonstrated in Figure 2. The relative uncertainty in E_{cut} is not just a simple function of ν . The smallest relative uncertainties are found for AGNs with constraints in the discarded $\tau_e > 3$ group, which contains targets over the full range of data quality, in particular those with high obscuring columns ($N_{\text{H}} > 10^{24} \text{ cm}^{-2}$; e.g., NGC 3281, NGC 6240) or prominent Compton humps ($R_{\text{pex}} > 1$; e.g., Mrk 1210, NGC 1194). Additional curvature due to these features makes spectra more susceptible to the $E_{\text{cut}}-\Gamma$ degeneracy.

Treating E_{cut} as a free parameter in spectral fitting results typically lowers the best-fit χ^2 compared to fixed $E_{\text{cut}} = 300 \text{ keV}$. However, in most cases, the reduction in χ^2 is not statistically significant because of the limited data quality and the fact that our analysis starts from a model that already fits the data well. Even in some cases of high-quality data, treating E_{cut} as a free parameter does not result in a significantly better fit because the uncertainty interval is consistent with 300 keV; such examples are NGC 2110 ($300_{-40}^{+50} \text{ keV}$) and NGC 4388 ($210_{-40}^{+120} \text{ keV}$). The lack of significant decreases in χ^2 simply justifies $E_{\text{cut}} = 300 \text{ keV}$ as a good assumption for the spectral analysis presented in Paper I. The majority of spectra that formally do not include 300 keV within the derived 68% uncertainty intervals belong to the discarded $\tau_e > 3$ group: 25 out of 44 in total. Of the 87 constraints with $\tau_e < 3$, 10 are above 300 keV, 9 are below, and 68 are consistent with this value given their 1σ uncertainties derived from XSPEC.

The typical E_{cut} constraint afforded by the spectral analysis of our sample is a lower limit in the 100–300 keV range. Excluding constraints with $E_{\text{cut}}^{\text{b.f.}}$ corresponding to $\tau_e > 3$ (the majority of which are full constraints) and the top third of our sample by data quality (accounting for 15 out of the remaining 20 full constraints), the rest of the sample yields E_{cut} constraints qualitatively similar to those shown in the middle and bottom panels of Figure 1. Stepping through the E_{cut} parameter space, χ^2 typically increases toward the lower end, and in some cases increases by a small amount above the best-fit value found in XSPEC. Our chosen confidence level (68%, corresponding to $\Delta\chi^2 = 1$) implies that typical constraints for any individual AGN should be considered with due caution. We note that despite the relatively low confidence level, for sample statistics such constraints are more informative than a smaller number of higher-confidence limits in the range of 30–100 keV.

Our sample also includes some strong constraints for bright AGNs. Three targets in our sample require E_{cut} other than 300 keV to reach χ^2 low enough to even consider the spectral model statistically acceptable based on the $p_{\text{null}} > 5\%$ criterion: MCG -05-023-16, NGC 5506, and Cen A. For a further three, NGC 262, NGC 7172, and ESO 103-G035, treating E_{cut} as a free parameter resulted in a significantly better fit. A notable improvement in best-fit χ^2 with free E_{cut} happens only in the cases where the spectrum is clearly more curved or clearly less curved than under the assumption of $E_{\text{cut}} = 300 \text{ keV}$. For four out of the six AGNs mentioned above, we find well-constrained E_{cut} in the 100–200 keV range. For the remaining two, fits imply $E_{\text{cut}} = 550_{-90}^{+140} \text{ keV}$ (Cen A) and $E_{\text{cut}} > 670 \text{ keV}$ (NGC 7172). More details on these extreme cases are given in the Appendix.

3.2. Distribution of E_{cut} in the Sample

The full distribution of constraints in the $E_{\text{cut}}-\Gamma$ plane obtained through our spectral analysis is shown in Figure 3. A

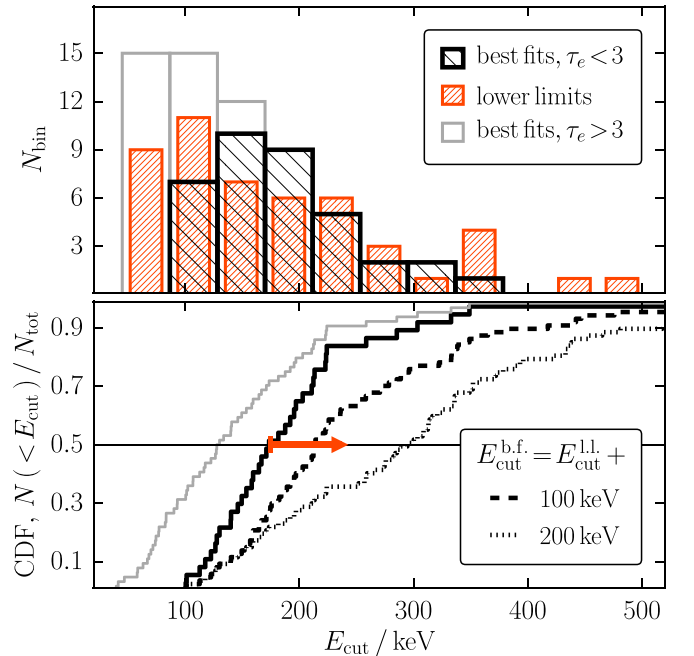


Figure 4. Top panel: histogram of the derived E_{cut} constraints for our sample. Best-fit values ($E_{\text{cut}}^{\text{b.f.}}$) are shown in black or gray, depending on τ_e calculated using Equation (3), while lower limits ($E_{\text{cut}}^{\text{l.l.}}$) are shown in red. Bottom panel: CDFs based only on $E_{\text{cut}}^{\text{b.f.}}$ including $\tau_e > 3$ constraints (gray) and excluding them (black). Due to numerous lower limits, these are actually lower bounds on the true CDF and its median (illustrated by the red rightward-pointing arrow). For comparison, we also show CDFs for the complete set of constraints under the simple assumptions that unconstrained $E_{\text{cut}}^{\text{b.f.}}$ are 100 and 200 keV above the measured $E_{\text{cut}}^{\text{l.l.}}$ (dashed and dotted black lines, respectively).

straightforward comparison with Figure 2 illustrates the direction of the degeneracy between these two parameters. After exclusion of E_{cut} constraints with $E_{\text{cut}}^{\text{b.f.}}$ corresponding to $\tau_e > 3$, which is shown with the solid blue line in Figure 3, our data set consists of 87 constraints in total. Of these, 37 include $E_{\text{cut}}^{\text{b.f.}}$, of which 20 are full constraints. For 50 cases we found only lower limits ($E_{\text{cut}}^{\text{l.l.}}$; at 68% confidence). This includes 11 constraints with only $E_{\text{cut}}^{\text{l.l.}}$ that formally fall in the $\tau_e > 3$ regime; as they correspond to upper limits on τ_e , they imply that τ_e in these cases is most likely lower.

In the top panel of Figure 4 we show a histogram of best-fit E_{cut} values ($E_{\text{cut}}^{\text{b.f.}}$) and lower limits ($E_{\text{cut}}^{\text{l.l.}}$) in cases where best-fit values are absent. Considering only best-fit values and neglecting any lower limits, the median of the E_{cut} distribution is 180 keV, with 68% of the distribution covering the range of 100–400 keV. Including all $E_{\text{cut}}^{\text{b.f.}}$ derived from spectral fitting, i.e., temporarily neglecting the $\tau_e < 3$ cut described in Section 2.3, would imply that the E_{cut} distribution median is 130 keV. However, these are clearly biased values failing to account for a considerable number of lower limits that suggest a higher median E_{cut} . This is illustrated in the bottom panel of Figure 4.

In order to incorporate numerous partial constraints into our estimate of the E_{cut} distribution, we employ a Monte Carlo bootstrapping method (e.g., Andrae 2010). We calculate a large number of cumulative distribution functions (CDFs) by resampling each E_{cut} constraint according to an approximate probability density function (PDF) that peaks at the best-fit value and contains 68% of the total probability within the 68% confidence interval determined from XSPEC. For lower limits,

we assume a particular PDF that contains 16% of the probability (as a one-sided tail outside of the central 68%) below $E_{\text{cut}}^{\text{ll}}$ determined from χ^2_{spec} . From a collection of 10,000 CDFs constructed in this way, we calculate the median CDF, which provides a more informed estimate of the median E_{cut} and the range containing 68% of the E_{cut} distribution. This procedure automatically provides a measure of uncertainty in these numbers based on the spread of the resampled CDFs. As with E_{cut} constraints, we quote uncertainties at the 1σ level and round them to the typical accuracy floor of 10 keV.

Our method requires an assumption of a PDF for resampling the constraints derived from spectral fitting. Taking into account the asymmetry of the likely PDFs for E_{cut} (demonstrated by the representative χ^2 curves shown in Figure 1), we adopt a PDF that consists of a Gaussian below $E_{\text{cut}}^{\text{b.f.}}$ and a Lorentzian above it. The latter provides a notably slower fall-off toward high energies. Both sides are scaled so that $E_{\text{cut}}^{\text{b.f.}}$ is the peak of the PDF and its width on each side matches the boundaries of the 68% uncertainty interval.²⁵ This choice is further supported by visual comparison with two PDFs determined from converged Markov Chain Monte Carlo (MCMC) chains shown in Figure 5. A two-sided Gaussian ($G|G$) is an excellent match in the well-constrained PDF for NGC 2110. However, including a Lorentzian tail to high energies ($G|L$) similar to the PDF for NGC 6300 is likely more appropriate for our sample given the generally lower reliability of $E_{\text{cut}}^{\text{u.l.}}$ determinations.

Lower limits are clearly less informative constraints, so we adopt a uniform distribution spanning a range of 300 keV in total. Its minimum is set so that 16% of probability is below the $E_{\text{cut}}^{\text{ll}}$ determined from spectral fitting. We treat partial constraints with both $E_{\text{cut}}^{\text{ll}}$ and $E_{\text{cut}}^{\text{b.f.}}$ values (but no upper limit on the confidence interval) as full constraints by assuming that $E_{\text{cut}}^{\text{u.l.}} = E_{\text{cut}}^{\text{b.f.}} + 150$ keV. The widths of these distributions are set conservatively based on widths of 68% confidence intervals for full constraints: the median width of $(E_{\text{cut}}^{\text{u.l.}} - E_{\text{cut}}^{\text{ll}})$ is 150 keV, while the maximum in our sample is approximately 300 keV. In Section 4.2 we discuss the effect of these choices on our results and consider alternatives.

The median of the E_{cut} distribution derived for our sample with the procedure and choices described above is 290 ± 20 keV. This uncertainty refers only to the median of the distribution and reflects only statistical uncertainty. The distribution itself is significantly wider, with 68% of the probability distribution spanning between 140 ± 10 keV and 540 ± 60 keV. The lower end of the 68% probability interval can be determined robustly, as it is largely independent of assumptions regarding partial constraints. The shape of the distribution, its median, and especially the upper end of the 68% probability interval depend to a certain extent on assumptions. For the remainder of the paper we adopt the sample and the analysis described here as fiducial. In the following sections we justify particular choices regarding our method, quantify known systematic uncertainties, and examine the effects of alternatives on the inferred E_{cut} distribution.

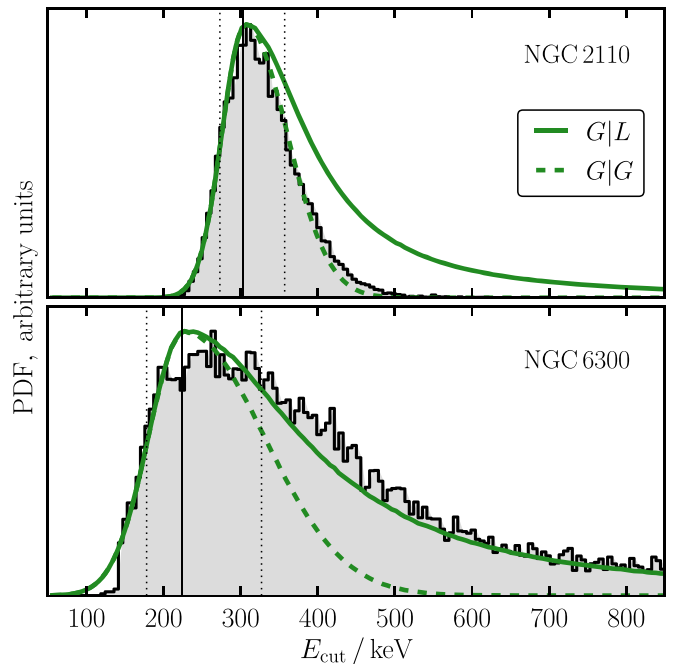


Figure 5. Two illustrative examples of PDFs derived from MCMC chains for two targets (NGC 2110 in the top panel, and NGC 6300 in the bottom panel), shown as gray histograms, compared to assumed analytic PDFs, shown with green curves. Solid lines show the adopted fiducial PDFs composed of a Gaussian and a Lorentzian ($G|L$), while the dashed lines show a two-sided Gaussian ($G|G$). In both cases, the transition occurs at the best-fit value ($E_{\text{cut}}^{\text{b.f.}}$; vertical solid line) and the standard deviation on either side is determined by the extent of the 68% confidence interval ($E_{\text{cut}}^{\text{ll}}$ and $E_{\text{cut}}^{\text{ul}}$; vertical dotted lines).

4. Discussion

4.1. Setting Expectations with Simulated Data

In order to better understand the results and justify some of the choices made for our fiducial analysis, we resort to simulations in which we control the input parameters. We simulate the whole measurement process under different assumptions following the procedure described below. The results are summarized in Figure 6.

For a fiducial model we adopted spectral parameters representative of our sample: $(\Gamma, R_{\text{pex}}, N_{\text{H}}/\text{cm}^{-2}, E_{\text{cut}}/\text{keV}) = (1.8, 0.5, 1.0 \times 10^{23}, 250)$. We set the flux to be representative of the sample median. In each realization, we simulated XRT and BAT spectra with typical exposures of 6 ks and 10 Ms, respectively, and NuSTAR spectra (both FPMA and FPMB) with exposures of 20, 50, and 100 ks. We then performed the same spectral analysis as on real data and collected E_{cut} constraints for each of the NuSTAR exposure lengths, as well as without any NuSTAR data (i.e., Swift data only). We repeated this procedure 100 times to approximately match our sample size. We then changed the value of one spectral parameter at a time, repeating the procedure for R_{pex} values of 0.1 and 2.0, N_{H} of $5 \times 10^{22} \text{ cm}^{-2}$ and $5 \times 10^{23} \text{ cm}^{-2}$, and E_{cut} set to 150 and 350 keV.

The simulations demonstrate the degree of systematic uncertainty in E_{cut} measurements for obscured AGNs. Almost independently of the amount of NuSTAR exposure and true underlying parameters of AGN spectra, the 68% spread in individual E_{cut} constraints is always large, typically $\gtrsim 100$ keV. This can be understood as a consequence of limited photon statistics in the highest-energy bins (as well as the highest-energy

²⁵ The Lorentzian formally has undefined moments, but its quantiles can be calculated from its CDF. The equivalent of 1σ corresponds to $1.817 \times \gamma$, where γ is the scale parameter of the distribution.

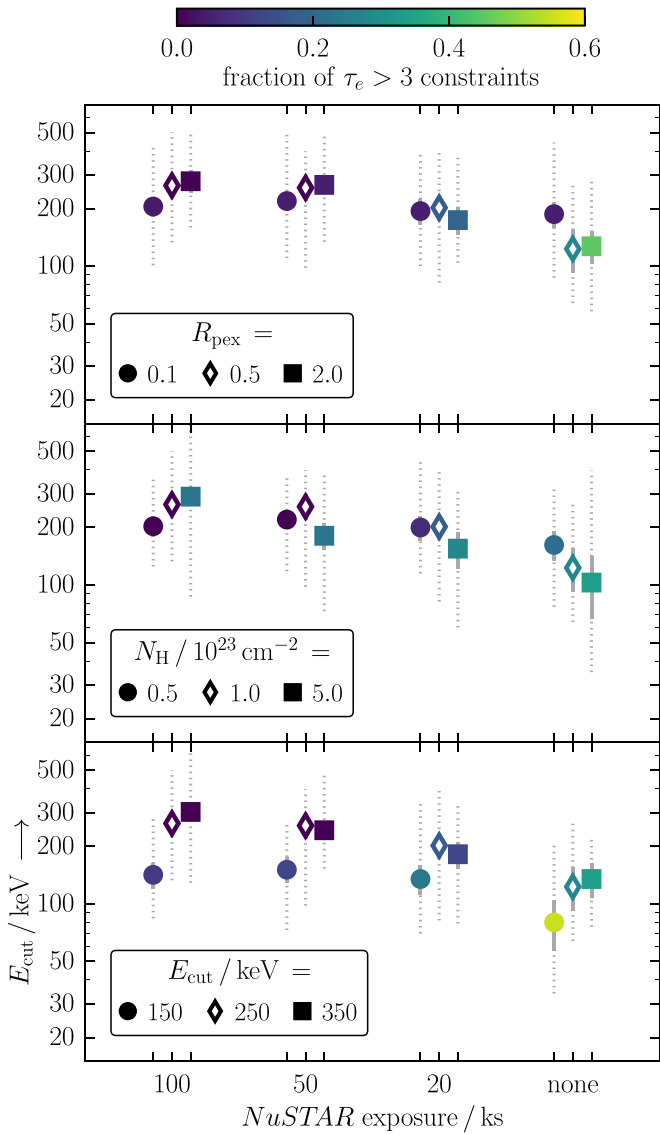


Figure 6. Results of spectral analysis on simulated data showing how the lack of NuSTAR data, as well as high values of R_{pex} and N_{H} , influences the estimate of E_{cut} . Solid error bars show the uncertainty in the median value based on 100 simulated measurements, while dotted error bars span the 68% probability interval for each sample. In each panel, the spectral parameter specified in the legend is varied as input for simulated data, which are then fitted to obtain E_{cut} constraints. For the reference model shown with open diamonds in each panel, we assumed the following parameters: $(\Gamma, R_{\text{pex}}, N_{\text{H}}/\text{cm}^{-2}, E_{\text{cut}}/\text{keV}) = (1.8, 0.5, 1.0 \times 10^{23}, 250)$. See Section 4.1 for a description of these simulations and a discussion of their implications.

Swift/BAT channels), since the measurement critically depends on subtle curvature at the high-energy end of the NuSTAR band. Any two measurements for the same input spectrum can differ significantly, so a single constraint should always be considered with caution. Inclusion of higher-quality NuSTAR data (or, equivalently, brighter targets) results in E_{cut} constraints that are both more accurate and more precise. However, even with long NuSTAR exposures on an AGN with our fiducial model spectrum ($E_{\text{cut}} = 250$ keV) and flux typical for our sample, the best-fit E_{cut} is expected to appear below 150 keV and above 450 keV in roughly 20% of individual measurements.

For the sample medians shown in Figure 6 we did not discard $\tau_e > 3$ constraints so as to demonstrate their impact.

Results of our simulations reveal several trends highlighted in Figure 6:

1. The fraction of spuriously inaccurate E_{cut} constraints corresponding to $\tau_e > 3$ is generally inversely proportional to the NuSTAR exposure.
2. A more pronounced Compton hump (greater R_{pex} parameter) tends to result in a higher fraction of $\tau_e > 3$ constraints, making the median E_{cut} biased toward low values. The effect decreases with increasing NuSTAR data quality.
3. High obscuration also makes E_{cut} constraints biased toward low values. Almost independently of NuSTAR data quality, a higher column density leads to more scatter in E_{cut} constraints and a higher proportion of $\tau_e > 3$ measurements.
4. Lower input E_{cut} values can be more accurately constrained, while higher values require higher data quality for the same relative accuracy. Also, a lower E_{cut} leads to a higher $\tau_e > 3$ fraction.

These simulation-based trends show that $\tau_e > 3$ constraints, especially those from pre-NuSTAR literature, are a natural consequence of limited data quality.

4.2. Systematic Uncertainties

As we have shown in the preceding section using simulated data, care should be taken in interpreting any one particular measurement for an individual AGN. However, the simulations also show that at the sample level effects of random under- and overestimates average out, allowing us to more reliably constrain the median of the intrinsic E_{cut} distribution. Our method of estimating the median of the E_{cut} distribution (Section 3.2) rests on certain assumptions; in this section we test them and discuss how our choices contribute to systematic uncertainties at the sample level. In Figure 7 we demonstrate the impact of a series of choices according to their effect on the CDF of the inferred E_{cut} distribution, from largest in the top panel to smallest in the bottom panel.

4.2.1. Choice of the PDFs

The largest contribution to systematic uncertainty in estimating the median E_{cut} is the choice of the range for uniform PDFs assumed for numerous lower limits. In order to demonstrate this, we define a scale parameter, q , so that uniform lower-limit PDFs span a range of $(q \times 300)$ keV, while for partial constraints (i.e., those lacking $E_{\text{cut}}^{\text{u.l.}}$) we assume $E_{\text{cut}}^{\text{u.l.}} = E_{\text{cut}}^{\text{b.f.}} + (q \times 150)$ keV. For our fiducial analysis presented in Section 3.2 we adopted $q = 1$. In the top panel of Figure 7 we show the effect of assuming a narrower range ($q = 0.5$) as well as a broader one ($q = 2$): the median E_{cut} in those cases shifts to 230 ± 10 keV and 390 ± 40 keV, respectively. Although arbitrary, we argue that $q \approx 1$ is a reasonable choice. A range much narrower than 300 keV would be overly optimistic given the spread in individual constraints found from simulations presented in Section 4.1. At the same time, a range of 300 keV is the maximum observed among individual full constraints in our sample.

The choice of PDF shape for both limits and full constraints affects the inferred E_{cut} distribution, but to a smaller extent. The effects of some alternative choices are shown in Figure 7,

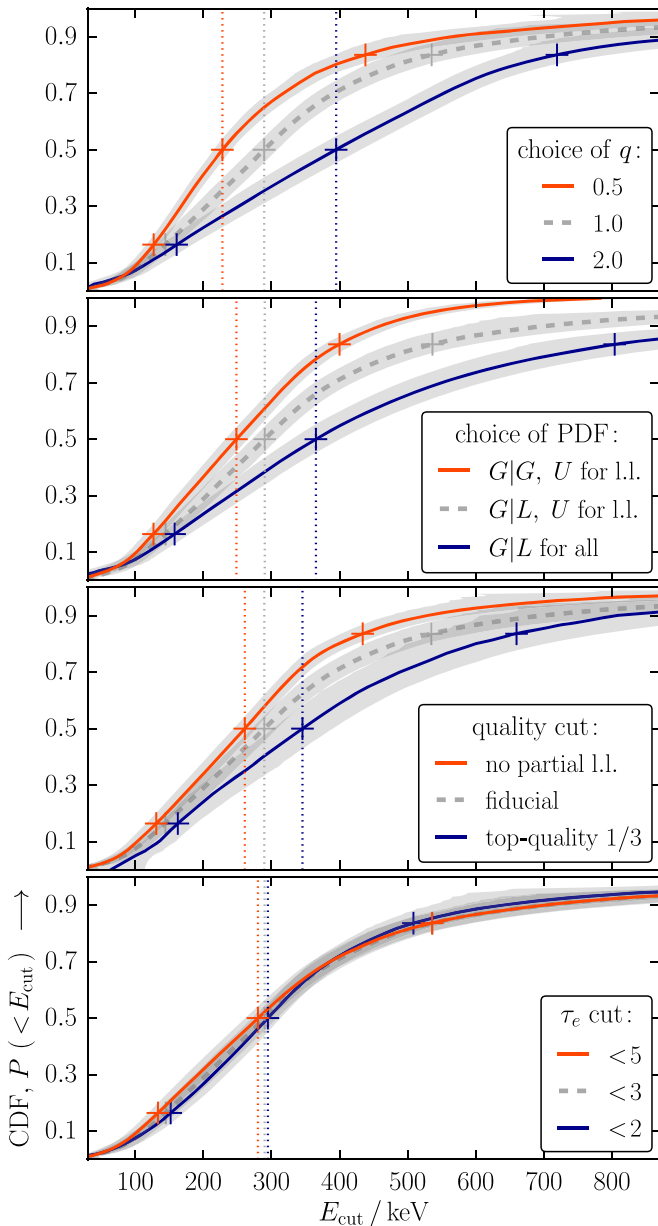


Figure 7. CDFs for E_{cut} under different assumptions. The fiducial distribution is reproduced in all panels as the thick gray dashed line. Gray areas surrounding each curve represent the 68% range occupied by randomized CDFs, constructed using the procedure described in Section 3.2. Solid lines show the median CDF in each case. Crosses intersecting each curve mark the median E_{cut} (emphasized with vertical dotted lines) and the 68% interval for each CDF. From top to bottom, panels illustrate the effects of varying the PDF scale parameter (q), changing the assumed shape of the PDFs, applying quality-based cuts, and different cuts in τ_e .

second panel from the top. The PDFs chosen for our fiducial analysis are uniform (U) for lower limits and a combination of a Gaussian (G ; below $E_{\text{cut}}^{\text{b.f.}}$) and a Lorentzian (L ; above $E_{\text{cut}}^{\text{b.f.}}$), designated as $G|L$ in Figure 7. If, instead, we employed a two-sided Gaussian ($G|G$) for full constraints, the PDF would be slightly narrower, and the sample median would shift to 250 ± 20 keV. This can be easily understood as a consequence of the stronger high-energy tail of the Lorentzian compared to the Gaussian. Because of numerous lower limits, changing their assumed PDF produces a slightly larger effect. One could assume the same $G|L$ combination for all constraints, in which

case $E_{\text{cut}}^{\text{b.f.}}$ for lower limits could be estimated as $E_{\text{cut}}^{\text{b.f.}} = E_{\text{cut}}^{\text{l.l.}} + q \times 150$ keV and they would be treated as partial constraints. The median E_{cut} would then shift to 360 ± 40 keV (assuming $q = 1$ as in the fiducial case), again owing to the long high-energy tail of the Lorentzian.

4.2.2. Cuts Based on Data Quality

We consider cuts directly related to data quality by dividing our sample into thirds according to the number of degrees of freedom as a proxy of overall data quality. For the top, middle, and bottom third of the sample, we obtain E_{cut} medians at 340 ± 40 keV, 310 ± 30 keV, and 230 ± 30 keV, respectively. This indicates that data quality has the tendency to lower the E_{cut} median, as expected from simulations presented in Section 4.1. Note that the fraction of $\tau_e > 3$ constraints does not strongly depend on data quality (21% for the top and bottom thirds, 29% for the middle third), but the fraction of lower limits does: it changes from 24% in the top third to 47% in the middle third and 61% in the bottom third. In the third panel from the top in Figure 7 we show the CDF constructed from the top third of the sample by data quality. The same panel also shows the effect of treating partial constraints (i.e., those lacking $E_{\text{cut}}^{\text{u.l.}}$ as lower limits instead of as full constraints. Because of their relatively small contribution, the effect on median E_{cut} is minor.

The effect of a different choice of a value for the cut in τ_e is small when applied to our sample. As shown in the bottom panel of Figure 7, the median E_{cut} would shift to 300 ± 20 keV and 280 ± 20 keV in the case of $\tau_e < 2$ and $\tau_e < 5$ cuts, respectively. With a cut in τ_e we might also be excluding AGNs that might have a genuinely low E_{cut} or an atypically hard intrinsic continuum ($\Gamma < 1.4$). Such examples have been found in analyses of a few type I AGNs with high-quality NuSTAR data (e.g., Kara et al. 2017; Tortosa et al. 2017; Turner et al. 2018). Since a complete removal of the cut would result in lowering our sample median by only 30 keV, we estimate that a small fraction of true low- E_{cut} AGNs would lower the median by ≤ 20 keV. We estimate that this fraction is low because our sample selection in the hard X-ray band is likely biased against AGNs with soft intrinsic continua and/or low E_{cut} .

4.2.3. Exclusion of Individual AGNs or Small Subsamples

This study is directed at constraining the typical E_{cut} in a sample representative of the Sy II population selected in the hard X-ray band. The size of our sample ensures that individual AGNs do not affect the result even for the extreme examples such as Cen A ($E_{\text{cut}} = 550_{-90}^{+140}$ keV), NGC 7172 ($E_{\text{cut}} > 670$ keV), or ESO 033-G002 ($E_{\text{cut}} > 460$ keV). Excluding all three lowers the median E_{cut} by < 10 keV. We further consider exclusion of small subsamples of AGNs that may be less representative of the Sy II population: those with potential contamination from a relativistic jet (broadly, *radio-loud* AGNs), and those with a detection of at least one broad line in their optical spectra (optical type 1.9). They are marked as members of these subsamples in Table 1; further details of their membership are discussed in Paper I. Excluding either of these subsamples, we find the median E_{cut} well within the statistical uncertainty for the full sample.

4.2.4. Alternative Estimation Method

Finally, we also test our results using independent and more commonly used tools of “survival analysis.” The Kaplan-Meier (KM) estimator adapted for analysis of univariate censored data in astronomy (Feigelson & Nelson 1985) is a part of the ASURV software package (Feigelson et al. 2014). The particular implementation we employ here is written in Python and was first used in the study by Shimizu et al. (2016). For our fiducial sample, the KM estimate of the E_{cut} mean is 270 keV, while the median is 230 keV. Since only best-fit values and lower limits are taken into account in these calculations, we estimate uncertainty on the median E_{cut} from a bootstrap procedure similar to our default method (except that there is no need to assume a PDF for lower limits). Due to the asymmetry of the assumed PDF for full constraints ($G|L$; see Figure 5), which gives more weight to higher energies, the median E_{cut} is then 260 ± 10 keV. The lower bound of the 68% interval is at 110 keV, with a statistical uncertainty smaller than 10 keV.

4.2.5. Summary of Systematic Uncertainties

From the analyses presented in Section 4.2, we conclude that the median E_{cut} for our Sy II sample can be constrained robustly based on our collection of individual E_{cut} constraints. We additionally verified, through simulations presented in Section 4.1 and tests on data for individual AGNs, that alternative choices of the fitting statistic and different data binning strategy do not systematically bias the sample-level results. Taking into account the examined systematics, we place the median E_{cut} at 290 ± 50 keV, where ± 20 keV is statistical uncertainty and ± 30 keV is added as estimated systematic uncertainty. We find that the lower bound of the 68% interval of the intrinsic E_{cut} distribution is relatively insensitive to various assumptions, placing it at 140 ± 20 keV (with statistical and systematic uncertainties approximately equal). The upper end of the E_{cut} distribution is clearly less constrained by our data and therefore depends heavily on assumptions. We estimate that the upper bound of the 68% interval is likely in the range of 400–600 keV.

4.3. Comparison with the Literature

4.3.1. Individual AGNs

For the majority of targets in our sample there are no strong constraints on E_{cut} in the literature, but there is some scope for comparison in the cases of relatively bright examples. In Table 2 we provide an overview of published E_{cut} constraints for 36 individual AGNs. The list is not exhaustive, as it only contains AGNs also present in our sample, but it provides an illustrative comparison. The table contains results from the largest samples of obscured AGNs studied to date, as well as studies of individual AGNs or small samples based on NuSTAR data. We limit listing results from Ricci et al. (2017) to targets that also have a constraint from another study; our overlap with their Swift/BAT sample is nearly complete, but the subset given in Table 2 is sufficiently illustrative. We only compare to results that included a spectral model equivalent to ours, i.e., including a reprocessing component such as `pexrav`.

A comparison of our results for individual AGNs with those from the pre-NuSTAR literature reveals a mix of consistent and inconsistent E_{cut} constraints. Table 2 highlights some patterns.

Of the 82 listed pre-NuSTAR constraints, 44 are lower limits that are generally consistent with our spectral fitting results. Of the remaining 38, only 12 are likely credible constraints according to our τ_e -based cut defined in Section 2.3, while the majority correspond to $\tau_e > 3$. Due to systematic uncertainties expected based on the simulations presented in Section 4.1, it is difficult to evaluate the significance of differences that could be ascribed to real spectral variability. In line with simulations, our results in the $\tau_e > 3$ regime tend to match the previous ones for AGNs with high obscuration ($\log N_{\text{H}}/\text{cm}^{-2} > 23.5$; e.g., Mrk 417, NGC 4507, NGC 4992), strong Compton humps ($R_{\text{pex}} \gtrsim 1$; e.g., Mrk 1210), a combination of both (e.g., NGC 3281), or simply limited-quality data (e.g., 2MASX J2330).

Comparing our spectral modeling results with previous constraints based on NuSTAR data reveals that they are not always consistent. For example, there is a stark difference for NGC 5506 ($E_{\text{cut}} = 110 \pm 10$ keV) in comparison to a slightly different spectral modeling of the same NuSTAR data by Matt et al. (2015), who argued that $E_{\text{cut}} > 350$ keV is a robust constraint (in lieu of the initial analysis, which yielded $E_{\text{cut}} = 720_{-190}^{+130}$ keV). Similarly, we find $E_{\text{cut}} = 550_{-90}^{+140}$ keV for Cen A, whereas Fürst et al. (2016) concluded that $E_{\text{cut}} > 1000$ keV. Both cases are discussed further in the Appendix, as are the differences for AGNs also studied by Rani et al. (2019) and other notably discrepant results. They clearly highlight the importance of acknowledging and quantifying systematics related to the choice of ancillary data and spectral model for any particular E_{cut} measurement even when high-quality NuSTAR data are used.

4.3.2. Sy II Samples

Studying broadband spectra of local AGNs with BeppoSAX, Dadina (2007, 2008) found that the average E_{cut} for their local Sy II sample is 380 ± 40 keV. This is based on 25 lower limits and only six full constraints, but the limits were incorporated into the calculation using the KM estimator. The average E_{cut} for the full sample (290 ± 20 keV) is less dominated by limits and therefore likely more reliable. Systematic uncertainties related to various assumptions (e.g., cross-normalization of nonoverlapping BeppoSAX instruments, handling of lower limits) were not considered in this work, making it appear that the relative uncertainty on the average E_{cut} is the same as in our case despite the smaller sample and lower-quality data. Nevertheless, the instantaneous broadband coverage, the similarity of the spectral model used for the analysis, and the use of censored statistics make this study most directly comparable to ours out of those currently in the literature.

Studying broadband X-ray spectra of obscured AGNs selected with INTEGRAL, de Rosa et al. (2012) obtained full constraints on E_{cut} for 10 targets, averaging 150 keV. The remainder of their sample (about two-thirds) yielded lower limits below 300 keV. Applying our method of estimating the median E_{cut} to constraints found by de Rosa et al. (2012) results in a median consistent with ours, especially if a $\tau_e < 3$ cut is applied as well. We note that about a third of their constraints fall in the $\tau_e > 3$ regime. This is consistent with our simulations presented in Section 4.1 for true E_{cut} in the range of 250–350 keV, with the caveat that our simulations assume lower-quality soft X-ray data. If the underlying population average were as low as 150 keV, the fraction of $\tau_e > 3$

Table 2
Comparison of Constraints on E_{cut} for Individual AGNs from the Literature

Target Name	$E_{\text{cut}}/\text{keV}$						
	This Work	D07	dR12	M13	V13	R17	NuSTAR [Reference]
NGC 262	170^{+40}_{-20}	(110^{+60}_{-30})	(80^{+40}_{-20}) [R19]
NGC 788	220^{+u}_{-100}	...	(60^{+40}_{-20})	>70	...
NGC 1365	290^{+200}_{-100}	>110	140^{+100}_{-60}	...
NGC 2110	300^{+50}_{-30}	>70	450 ± 60	320^{+100}_{-60} [U19]
Mrk 3	150^{+70}_{-30}	>190	>200	>450	...
Mrk 1210	(90^{+30}_{-20})	>110	>120	...
MCG -01-24-012	110^{+60}_{-30}	>420	(80^{+90}_{-30})	...
NGC 2992	>380	150^{+170}_{-50}	(60^{+40}_{-20})	150^{+130}_{-70} [R19]
MCG -05-23-016	150^{+10}_{-20}	190^{+10}_{-60}	>170	(70^{+150}_{-30})	...	100 ± 10	120 ± 10 [B15]
ESO 263-G013	>120	...	>150	>60	...
Mrk 417	(130^{+110}_{-50})	(40^{+10}_{-20})	>120	...
NGC 3281	(70^{+20}_{-10})	(70 ± 30)	>60	(40^{+120}_{-20})	...	(60^{+20}_{-10})	...
NGC 4258	>180	>280	>310	...
NGC 4388	210^{+120}_{-40}	>460	>180	200^{+200}_{-150}	$\gg 200$	>100	200^{+80}_{-40} [U19]
NGC 4395	(120^{+50}_{-30})	(50^{+30}_{-10})	>260	...
NGC 4507	(80^{+10}_{-20})	>80	130^{+150}_{-50}	>60	...	130^{+90}_{-40}	...
LEDA 170194	>230	...	>210	>200	...
NGC 4945	>240	120^{+40}_{-30}	>80	100^{+260}_{-60}	...	>40	190^{+200}_{-40} [P14]
NGC 4992	(80^{+100}_{-30})	...	(110^{+190}_{-20})	(70^{+140}_{-30})	...
Cen A	550^{+140}_{-90}	>250	>400	(70 ± 10)	>1000 [F16]
NGC 5252	330^{+50}_{-100}	...	>50	...	110^{+60}_{-20}	(80 ± 10)	...
NGC 5506	110 ± 10	>180	...	>90	170^{+110}_{-30}	130 ± 10	>350 [M15]
NGC 5899	>340	>210	>40	...
IC 4518A	120^{+160}_{-50}	...	(70^{+60}_{-30})	(20^{+60}_{-10})	...	(70^{+330}_{-30})	...
Mrk 1498	(60 ± 10)	(70^{+90}_{-20})	(80^{+50}_{-20}) [U18]
ESO 137-G034	>160	...	>150	>230	...
NGC 6300	210^{+100}_{-50}	...	>250	>520	...	(80^{+30}_{-20})	...
2MASX J2018	170^{+u}_{-70}	...	(50^{+110}_{-20})	>60	...
ESO 103-G035	100^{+20}_{-10}	...	(50^{+250}_{-30})	>30	...	(60^{+20}_{-10})	100^{+90}_{-30} [B18]
Cyg A	130^{+70}_{-30}	(100^{+20}_{-10})	>110 [R15]
MCG +04-48-002	>150	...	>180	>60	...
NGC 7172	>670	>40	(70 ± 10)	(110 ± 20)	(70 ± 10) [R19]
NGC 7582	200^{+190}_{-80}	>50	>130	...
2MASX J2330	>70	...	(60^{+340}_{-40})	>90	...
PKS 2331-240	220^{+u}_{-110}	>250 [U18]
PKS 2356-61	160^{+u}_{-80}	>50	>60 [U18]

Note. Targets highlighted with bold font are discussed individually in the [Appendix](#). Constraints in parentheses correspond to $\tau_e > 3$, calculated using Equation (3).
References. D07 = Dadina (2007); dR12 = de Rosa et al. (2012); M13 = Molina et al. (2013); V13 = Vasudevan et al. (2013); P14 = Puccetti et al. (2014); B15 = Baloković et al. (2015); M15 = Matt et al. (2015); R15 = Reynolds et al. (2015); F16 = Fürst et al. (2016); R17 = Ricci et al. (2017); B18 = Buisson et al. (2018); U18 = Ursini et al. (2018a); R19 = Rani et al. (2019); U19 = Ursini et al. (2019).

constraints in their sample would likely be higher ($\gtrsim 50\%$; see Figure 6).

Ricci et al. (2017) derived E_{cut} constraints for many Swift/BAT-selected AGNs (including most of our sample) using only Swift/BAT data in the hard X-ray band. As the majority of their constraints are lower limits, they employed a Monte Carlo scheme similar to ours in order to estimate the sample median. The main difference is the fixed upper end of the energy range for the uniform PDF assumed for lower limits instead of our scale parameter q defined in Section 4.2. Assuming uniform PDFs extending up to 1000 keV, for obscured AGNs ($\log N_{\text{H}}/\text{cm}^{-2} > 22$) Ricci et al. (2017) found the E_{cut} median at 380 ± 20 keV. Replacing 1000 keV with 500 keV, which more closely corresponds to our $q = 1$ assumption, lowered the median for the full sample to 240 ± 10 keV. As a further

check, they employed a KM estimator, finding the median E_{cut} for obscured AGNs to be 190 ± 30 keV. These calculations include $\tau_e > 3$ constraints that our analysis would have excluded. Neglecting the τ_e -based cut lowers our median by about 30 keV, so it is reasonable to expect that incorporating such a cut would increase their estimates by at least as much. We base this estimate on the higher expected and observed fraction of $\tau_e > 3$ constraints in their sample ($\simeq 35\%$) compared to Figure 6, keeping in mind the assumed lower quality of soft X-ray data in our simulations.

Most other studies of obscured AGN samples are less directly comparable with ours. From spectral analysis of stacked INTEGRAL data for a local Sy II sample, Ricci et al. (2011) found $E_{\text{cut}} = 150^{+190}_{-80}$ keV. Subdividing their sample by obscuration and using a model that includes a pexrav

component, they constrained E_{cut} to 430^{+270}_{-120} keV for AGNs obscured by column density $\log N_{\text{H}}/\text{cm}^{-2} < 23$ and 290^{+110}_{-60} keV for AGNs with $23 < \log N_{\text{H}}/\text{cm}^{-2} < 24$. Our simulations (Section 4.1) suggest that such a trend might arise artificially, as E_{cut} is simply more difficult to constrain at high obscuration owing to the greater parameter degeneracy. For the same subdivision by column density but using stacked Swift/BAT data, Esposito & Walter (2016) successfully modeled both classes assuming $E_{\text{cut}} = 250$ keV, finding a 68% lower limit around 180 keV.

4.3.3. Sy I and Mixed Samples

Studies of the E_{cut} distribution in unobscured and type 1 AGNs (jointly referred to as Sy I here) have previously been carried out using BeppoSAX, INTEGRAL, and Swift data covering the hard X-ray band. Typically focusing on samples of up to a few dozen targets, studies like Perola et al. (2002), Panessa et al. (2008), and Vasudevan et al. (2013), for example, found a spread between 50 and roughly 500 keV. Analyses of stacked INTEGRAL data (Ricci et al. 2011) and stacked Swift/BAT data for the INTEGRAL-selected sample (Esposito & Walter 2016) both found the average E_{cut} to be above 150 keV. In a study of the average broadband X-ray AGN spectrum (constrained by luminosity functions in different X-ray bands), Ballantyne (2014) indirectly found $E_{\text{cut}} = 270^{+170}_{-80}$ keV.

Molina et al. (2013) studied constraints from both INTEGRAL and Swift/BAT data, estimating that the average E_{cut} over both types is in the 200–220 keV range (with a spread of several hundred keV) when lower limits are considered and $\tau_e > 3$ constraints are included. The study of Ricci et al. (2017) resulted in a large collection of E_{cut} constraints for Swift/BAT-selected AGNs of all types. They found the median E_{cut} for the whole sample to be in the range of 240–380 keV depending on the assumed upper end of uniform PDFs for lower limits (500–1000 keV). Note that $q = 1$ adopted for our fiducial analysis is more directly comparable to the lower end of that range, and that this median estimate would have likely been higher had $\tau_e > 3$ constraints been excluded.

Not all broadband X-ray studies of obscured and unobscured AGN samples in the literature found a population-average E_{cut} consistent with our median. While some authors claimed that the average E_{cut} is likely higher than the energy range of most X-ray instruments, above 200 keV (e.g., Dadina 2008; Vasudevan et al. 2013; Ricci et al. 2018), others concluded that the average is likely below 150 keV (e.g., Molina et al. 2009; Malizia et al. 2014). Recent work by Molina et al. (2019), based on NuSTAR data for the INTEGRAL-selected type 1 AGN sample previously studied by the authors, confirmed their earlier results. An independent study of a different sample by Rani et al. (2019) claimed a similarly low average E_{cut} . These results pointing to the typical E_{cut} below 150 keV in Sy I samples are apparently inconsistent with our result for the Sy II population. Since they do not suffer from lower hard X-ray data quality as pre-NuSTAR studies do, this may be indicative of an emerging difference in future studies that will include a more detailed consideration of potential biases.

Within the framework of the orientation-based Unified Model for AGNs (Antonucci 1993; Urry & Padovani 1995), differences in coronal spectra can be expected if the AGN corona has a net velocity perpendicular to the accretion disk, possibly related to the formation of a relativistic jet (e.g., Malzac et al. 2001; Markoff et al. 2005; Liu et al. 2014). With

the data presented herein, the estimated systematic uncertainty in the median E_{cut} of our sample, and the results currently in the literature, it is not possible to firmly establish whether the E_{cut} distributions in Sy I (largely unobscured) and Sy II (largely obscured) populations in the local universe are significantly different or not. This would require a detailed account of systematic uncertainties and selection biases, which is beyond the scope of this paper. For example, our sample selection in the hard X-ray band is likely biased against Sy II with soft intrinsic continua (as counterparts of the narrow-line Sy I population; e.g., Boller et al. 1996), but their share in the Sy II population is currently unknown. Furthermore, there are several limitations of our current spectral analysis that can be improved on in future work, thus enabling reliable comparisons between different subclasses. We describe some of them in the following section.

4.4. Limitations and Future Work

The data presented here are from single-epoch, short, simultaneous NuSTAR and Swift/XRT observations, aided with Swift/BAT data integrated over 70 months. An increase in NuSTAR exposure from the typical 20 ks exposure presented here to 50 ks or 100 ks is achievable for a subset of our sample and would yield improvement approximately summarized in Figure 6. Analyses of multiepoch data for selected unobscured (e.g., Turner et al. 2018) and obscured AGNs (e.g., Buisson et al. 2018) already provided improved constraints on spectral parameters of the coronal emission and uncovered their variability (e.g., Zoghbi et al. 2017; Ursini et al. 2018b; Zhang et al. 2018). AGNs are well known to be variable, and additional multiepoch NuSTAR data would enable studies of variability in the physical parameters of the corona, the innermost parts of the accretion flow, and their scaling relations (e.g., Keek & Ballantyne 2016).

An important consideration for characterizing coronae of obscured AGNs is that the shape of the reprocessed continuum—specifically, the Compton hump—is fixed in the analysis presented here. For simplicity, we neglected possible contributions from relativistically broadened reprocessing in the inner accretion disk, focusing only on reprocessing ascribed to the larger-scale obscuring torus, although both could be contributing to the X-ray spectra of obscured AGNs (e.g., Guainazzi et al. 2010; Xu et al. 2017; Walton et al. 2019). Despite its popularity in the literature, the `perxav` model we employed here does not have the correct geometry to properly represent the torus. Spectral models for reprocessing in the torus exhibit a greater range in the shape and amplitude of the Compton hump (e.g., Paltani & Ricci 2017; Buchner et al. 2019; Tanimoto et al. 2019). In future publications we will use modern spectral models from the BORUS suite (Baloković et al. 2018, 2019) that self-consistently account for the cutoff in the coronal continuum, as well as the reprocessing features from the torus.

The simple power law with an exponential cutoff is often used in X-ray spectral analyses, and as such it is important for characterization of the average AGN spectrum (e.g., for CXB modeling). However, it is not an accurate representation of the AGN coronal spectrum (e.g., Fabian et al. 2015; Lubiński et al. 2016; Niedźwiecki et al. 2019). Although the phenomenological parameter E_{cut} may be approximately converted to a coronal temperature under certain assumptions (Middei et al. 2019), the proper way to characterize the physical parameters of obscured AGN coronae is to directly employ more

physically motivated spectral models for coronal emission. This will enable more straightforward comparison between coronae of obscured and unobscured AGNs, their physical properties, and possibly scaling relations and evolution (e.g., Kammoun et al. 2017; Lanzuisi et al. 2019). More similar studies are expected in the future based on NuSTAR data, though higher-sensitivity and higher-energy coverage of the proposed missions HEX-P (Madsen et al. 2018, 2019) or FORCE (Nakazawa et al. 2018) will be needed in order to reach large AGN samples and detailed coronal physics (Kamraj et al. 2019).

The authors appreciate helpful suggestions from the anonymous referee, which helped to improve the clarity of the paper.

M.B. acknowledges support from the YCAA Prize Postdoctoral Fellowship, the National Aeronautics and Space Administration (NASA) under the NASA Earth and Space Science Fellowship program (grant NNX14AQ07H), and support from the Black Hole Initiative at Harvard University, which is funded in part by the Gordon and Betty Moore Foundation (grant GBMF8273) and in part by the John Templeton Foundation. A.C. and G.M. acknowledge support from the ASI/INAF grant I/037/12/0 and the Caltech Kingsley fellowship program. A.A. acknowledges financial support from Ministry of Education Malaysia Fundamental Research Grant Scheme grant code FRGS/1/2019/STG02/UKM/02/7. P.B. acknowledges financial support from the STFC and the Czech Science Foundation project No. 19-05599Y. P.G. acknowledges support from the STFC and a UGC/UKIERI Thematic Partnership.

We have made use of data from the NuSTAR mission, a project led by the California Institute of Technology, managed by the Jet Propulsion Laboratory, and funded by the National Aeronautics and Space Administration. We thank the NuSTAR Operations, Software and Calibration teams for support with the execution and analysis of these observations. This research has made use of the NuSTAR Data Analysis Software (NuSTARDAS) jointly developed by the Space Science Data Center (SSDC; ASI, Italy) and the California Institute of Technology (USA). Part of this work is based on archival data, software, or online services provided by the SSC. This research has made use of the High Energy Astrophysics Science Archive Research Center Online Service, provided by the NASA/Goddard Space Flight Center and NASA’s Astrophysics Data System.

Facilities: NuSTAR, Swift.

Software: Astropy (Astropy Collaboration et al. 2013, 2018), ASURV (Feigelson et al. 2014), Matplotlib (Hunter 2007), Xspec (Arnaud 1996).

Appendix Notes on Particular Targets

NGC 2110.—While the high- E_{cut} constraint from Ricci et al. (2017) is not strongly inconsistent with our analysis, we confirm that our lower NuSTAR-based constraint is robust despite achieving no improvement in terms of χ^2 reduction with respect to modeling presented in Paper I. Using INTEGRAL data and two epochs of NuSTAR data in the hard X-ray band, Ursini et al. (2019) affirm our result, surpassing an earlier lower limit (>210 keV) found by Marinucci et al. (2015).

NGC 2992.—NuSTAR observation of this target was taken at a time when its hard X-ray flux was more than a factor of 5 higher than the long-term average probed by Swift/BAT. High flux was also identified in the multiepoch spectral analysis by Marinucci et al. (2018), which yielded $E_{\text{cut}} > 350$ keV. Excluding the highly offset Swift/BAT data results in an even higher lower limit, we find $E_{\text{cut}} > 490$ keV. Lowering E_{cut} manually, we find that statistically acceptable models ($p_{\text{null}} > 5\%$) can be found down to 80 keV (formally consistent with the result from Rani et al. 2019), albeit with clear excess in residuals at the high-energy end of the NuSTAR bandpass.

MCG –05-23-016.—In addition to the NuSTAR-based study of Baloković et al. (2015) listed in Table 2, NuSTAR data for this bright target were also analyzed by Zoghbi et al. (2017) and Tortosa et al. (2018b). While each of those analyses implies a different E_{cut} owing to details of data selection and spectral models used for fitting, there is agreement that in this case E_{cut} is likely $\lesssim 150$ keV, i.e., low enough that NuSTAR data constrain it well.

NGC 4388.—For this target our constraint agrees very well with a more detailed study by Ursini et al. (2019), including NuSTAR and INTEGRAL hard X-ray data. We also confirm $E_{\text{cut}} \approx 200$ keV from a dedicated multiepoch study with a different spectral model (M. Baloković et al. 2020, in preparation). The data used in our analysis do not strongly reject E_{cut} above lower limits found by de Rosa et al. (2012) and Vasudevan et al. (2013), as an acceptable model with $p_{\text{null}} > 5\%$ can be found as long as $E_{\text{cut}} > 160$ keV.

Cen A.—The discrepancy between the Swift/BAT-based constraint from Ricci et al. (2017), which is in the $\tau_e > 3$ regime (70 ± 10 keV), and nearly all other studies implying a very high E_{cut} (including this paper and Fürst et al. 2016, based on high-quality NuSTAR data) is probably the best example of the spurious occurrence of degenerate $\tau_e > 3$ constraints. The cause for this may be the curvature of the Swift/BAT spectrum, which does not match the very flat NuSTAR spectrum. For this reason we excluded Swift/BAT data from our fitting already in Paper I, as it was impossible to find an acceptable model otherwise. The extremely high E_{cut} may be indicative of a contribution from the relativistic jet in this AGN, so we test its exclusion from the sample in Section 4.2.3, finding negligible impact on the population median.

NGC 5506.—Initial analysis of NuSTAR data for this target by Matt et al. (2015), as well as a reanalysis by Tortosa et al. (2018b) using a slightly different spectral model (replacing the `pexrav` component with the `xillver` model from García et al. 2013, which self-consistently includes fluorescent line emission), yielded a constraint on E_{cut} far above the NuSTAR band, at ≈ 700 keV. A more robust lower limit, found by considering alternative models, was found to be >350 keV. However, E_{cut} in that range is inconsistent with the highly curved Swift/BAT spectrum. Excluding it from our fitting, we find $E_{\text{cut}} = 210_{-30}^{+120}$ keV. Also excluding Swift/BAT data and using spectral models self-consistently accounting for coronal emission and reprocessing, Baloković et al. (2019) found kT_e in the 70–110 keV range (depending on the chosen model), which corresponds to $E_{\text{cut}} \approx 140$ –330 keV assuming the simple conversion from Equation (1).

NGC 6300.—The only apparent discrepancy in constraints for this target is with respect to joint modeling of INTEGRAL and Swift/BAT spectra by Molina et al. (2013). The high lower limit (>520 keV) is based on their modeling with a free R_{pex}

parameter and is likely spurious. From fits with R_{pex} fixed at 0, 1, and 2, they derive E_{cut} in the range of 40–90 keV, all of which correspond to $\tau_e > 3$.

NGC 7172.—Removing the Swift/BAT data from the fit does not change the high lower limit on E_{cut} , and neither does further exclusion of Swift/XRT data. We find a more robust lower limit, such that no models meet the $p_{\text{null}} > 5\%$ criterion below it, at $E_{\text{cut}} > 250$ keV. We are unable to match the data with the spectral parameters listed by Rani et al. (2019), who constrained E_{cut} to 70 ± 10 keV based on NuSTAR data alone. A similarly low and tight E_{cut} constraint was found by de Rosa et al. (2012) from nonsimultaneous and nonoverlapping XMM-Newton and INTEGRAL data. In both cases these constraints correspond to $\tau_e > 3$.

ORCID iDs

M. Baloković  <https://orcid.org/0000-0003-0476-6647>

F. A. Harrison  <https://orcid.org/0000-0003-2992-8024>

A. Comastri  <https://orcid.org/0000-0003-3451-9970>

C. Ricci  <https://orcid.org/0000-0001-5231-2645>

A. Annuar  <https://orcid.org/0000-0003-0387-1429>

D. R. Ballantyne  <https://orcid.org/0000-0001-8128-6976>

P. Boorman  <https://orcid.org/0000-0001-9379-4716>

W. N. Brandt  <https://orcid.org/0000-0002-0167-2453>

M. Brightman  <https://orcid.org/0000-0002-8147-2602>

P. Gandhi  <https://orcid.org/0000-0003-3105-2615>

N. Kamraj  <https://orcid.org/0000-0002-3233-2451>

M. J. Koss  <https://orcid.org/0000-0002-7998-9581>

S. Marchesi  <https://orcid.org/0000-0001-5544-0749>

A. Marinucci  <https://orcid.org/0000-0002-2055-4946>

A. Masini  <https://orcid.org/0000-0002-7100-9366>

G. Matt  <https://orcid.org/0000-0002-2152-0916>

D. Stern  <https://orcid.org/0000-0003-2686-9241>

C. M. Urry  <https://orcid.org/0000-0002-0745-9792>

References

- Ajello, M., Costamante, L., Sambruna, R. M., et al. 2009, *ApJ*, 699, 603
- Akylas, A., Georgakakis, A., Georgantopoulos, I., Brightman, M., & Nandra, K. 2012, *A&A*, 546, A98
- Ananna, T. T., Treister, E., Urry, C. M., et al. 2019, *ApJ*, 871, 240
- Andrae, R. 2010, arXiv:1009.2755
- Antonucci, R. 1993, *ARA&A*, 31, 473
- Arnaud, K. A. 1996, in ASP Conf. Ser. 101, *Astronomical Data Analysis Software and Systems V*, ed. G. H. Jacoby & J. Barnes (San Francisco, CA: ASP), 17
- Astropy Collaboration, Price-Whelan, A. M., Sipőcz, B. M., et al. 2018, *AJ*, 156, 123
- Astropy Collaboration, Robitaille, T. P., Tollerud, E. J., et al. 2013, *A&A*, 558, A33
- Axelsson, M., Hjalmarsson, L., & Done, C. 2013, *MNRAS*, 431, 1987
- Ballantyne, D. R. 2014, *MNRAS*, 437, 2845
- Baloković, M. 2017, PhD thesis, California Institute of Technology, doi:10.7907/Z9WM1BG8
- Baloković, M., Brightman, M., Harrison, F. A., et al. 2018, *ApJ*, 854, 42
- Baloković, M., García, J. A., & Cabral, S. E. 2019, *RNAAS*, 3, 173
- Baloković, M., Matt, G., Harrison, F. A., et al. 2015, *ApJ*, 800, 62
- Baumgartner, W. H., Tueller, J., Markwardt, C. B., et al. 2013, *ApJS*, 207, 19
- Boller, T., Brandt, W. N., & Fink, H. 1996, *A&A*, 305, 53
- Buchner, J., Brightman, M., Nandra, K., Nikutta, R., & Bauer, F. E. 2019, *A&A*, 629, A16
- Buchner, J., Georgakakis, A., Nandra, K., et al. 2015, *ApJ*, 802, 89
- Buisson, D. J. K., Fabian, A. C., & Lohfink, A. M. 2018, *MNRAS*, 481, 4419
- Chartas, G., Rhea, C., Kochanek, C., et al. 2016, *AN*, 337, 356
- Comastri, A., Setti, G., Zamorani, G., & Hasinger, G. 1995, *A&A*, 296, 1
- Dadina, M. 2007, *A&A*, 461, 1209
- Dadina, M. 2008, *A&A*, 485, 417
- De Marco, B., Ponti, G., Cappi, M., et al. 2013, *MNRAS*, 431, 2441
- de Rosa, A., Panessa, F., Bassani, L., et al. 2012, *MNRAS*, 420, 2087
- Draper, A. R., & Ballantyne, D. R. 2009, *ApJ*, 707, 778
- Esposito, V., & Walter, R. 2016, *A&A*, 590, A49
- Fabian, A. C., Lohfink, A., Kara, E., et al. 2015, *MNRAS*, 451, 4375
- Feigelson, E. D., & Nelson, P. I. 1985, *ApJ*, 293, 192
- Feigelson, E. D., Nelson, P. I., Isobe, T., & LaValley, M. 2014, ASURV: Astronomical SURVival Statistics, Astrophysics Source Code Library, ascl:1406.001
- Fürst, F., Müller, C., Madsen, K. K., et al. 2016, *ApJ*, 819, 150
- Gandhi, P., Fabian, A. C., Suebsuwong, T., et al. 2007, *MNRAS*, 382, 1005
- García, J., Dauser, T., Reynolds, C. S., et al. 2013, *ApJ*, 768, 146
- Gilli, R., Comastri, A., & Hasinger, G. 2007, *A&A*, 463, 79
- Gondek, D., Zdziarski, A. A., Johnson, W. N., et al. 1996, *MNRAS*, 282, 646
- Guainazzi, M., Bianchi, S., Matt, G., et al. 2010, *MNRAS*, 406, 2013
- Guerras, E., Dai, X., Steele, S., et al. 2017, *ApJ*, 836, 206
- Haardt, F., & Maraschi, L. 1991, *ApJL*, 380, L51
- Harrison, F. A., Craig, W. W., Christensen, F. E., et al. 2013, *ApJ*, 770, 103
- Hickox, R. C., & Alexander, D. M. 2018, *ARA&A*, 56, 625
- Hunter, J. D. 2007, *CSE*, 9, 90
- Kammoun, E. S., Risaliti, G., Stern, D., et al. 2017, *MNRAS*, 465, 1665
- Kamraj, N., Fabian, A., Lohfink, A., et al. 2019, *BAAS*, 51, 126
- Kamraj, N., Harrison, F. A., Baloković, M., Lohfink, A., & Brightman, M. 2018, *ApJ*, 866, 124
- Kara, E., Alston, W. N., Fabian, A. C., et al. 2016, *MNRAS*, 462, 511
- Kara, E., García, J. A., Lohfink, A., et al. 2017, *MNRAS*, 468, 3489
- Keek, L., & Ballantyne, D. R. 2016, *MNRAS*, 456, 2722
- Koss, M., Trakhtenbrot, B., Ricci, C., et al. 2017, *ApJ*, 850, 74
- Lanzuisi, G., Gilli, R., Cappi, M., et al. 2019, *ApJL*, 875, L20
- Liu, T., Wang, J.-X., Yang, H., Zhu, F.-F., & Zhou, Y.-Y. 2014, *ApJ*, 783, 106
- Lubiński, P., Beckmann, V., Gibaud, L., et al. 2016, *MNRAS*, 458, 2454
- Ludlam, R. M., Cackett, E. M., Gültekin, K., et al. 2015, *MNRAS*, 447, 2112
- Madsen, K., Hickox, R., Bachetti, M., et al. 2019, *BAAS*, 51, 166
- Madsen, K. K., Harrison, F., Broadway, D., et al. 2018, *Proc. SPIE*, 10699, 106996M
- Magdziarz, P., & Zdziarski, A. A. 1995, *MNRAS*, 273, 837
- Malizia, A., Molina, M., Bassani, L., et al. 2014, *ApJL*, 782, L25
- Malzac, J., Beloborodov, A. M., & Poutanen, J. 2001, *MNRAS*, 326, 417
- Marinucci, A., Bianchi, S., Braito, V., et al. 2018, *MNRAS*, 478, 5638
- Marinucci, A., Matt, G., Bianchi, S., et al. 2015, *MNRAS*, 447, 160
- Markoff, S., Nowak, M. A., & Wilms, J. 2005, *ApJ*, 635, 1203
- Matt, G., Baloković, M., Marinucci, A., et al. 2015, *MNRAS*, 447, 3029
- McHardy, I. M. 2013, *MNRAS*, 430, L49
- Merloni, A., & Fabian, A. C. 2003, *MNRAS*, 342, 951
- Middei, R., Bianchi, S., Marinucci, A., et al. 2019, *A&A*, 630, A131
- Molina, M., Bassani, L., Malizia, A., et al. 2009, *MNRAS*, 399, 1293
- Molina, M., Bassani, L., Malizia, A., et al. 2013, *MNRAS*, 433, 1687
- Molina, M., Malizia, A., Bassani, L., et al. 2019, *MNRAS*, 484, 2735
- Mosquera, A. M., Kochanek, C. S., Chen, B., et al. 2013, *ApJ*, 769, 53
- Nakazawa, K., Mori, K., Tsuru, T. G., et al. 2018, *Proc. SPIE*, 10699, 106992D
- Niedźwiecki, A., Szanecki, M., & Zdziarski, A. A. 2019, *MNRAS*, 485, 2942
- Osterbrock, D. E. 1981, *ApJ*, 249, 462
- Paltani, S., & Ricci, C. 2017, *A&A*, 607, A31
- Panessa, F., Bassani, L., de Rosa, A., et al. 2008, *A&A*, 483, 151
- Perola, G. C., Matt, G., Cappi, M., et al. 2002, *A&A*, 389, 802
- Petrucci, P. O., Haardt, F., Maraschi, L., et al. 2001, *ApJ*, 556, 716
- Poutanen, J., & Svensson, R. 1996, *ApJ*, 470, 249
- Puccetti, S., Comastri, A., Fiore, F., et al. 2014, *ApJ*, 793, 26
- Rani, P., Stalin, C. S., & Goswami, K. D. 2019, *MNRAS*, 484, 5113
- Reynolds, C. S., Lohfink, A. M., Ogle, P. M., et al. 2015, *ApJ*, 808, 154
- Ricci, C., Ho, L. C., Fabian, A. C., et al. 2018, *MNRAS*, 480, 1819
- Ricci, C., Trakhtenbrot, B., Koss, M. J., et al. 2017, *ApJS*, 233, 17
- Ricci, C., Walter, R., Courvoisier, T. J.-L., & Paltani, S. 2011, *A&A*, 532, A102
- Rivers, E., Markowitz, A., & Rothschild, R. 2011, *ApJS*, 193, 3
- Rothschild, R. E., Mushotzky, F. R., Baity, W. A., et al. 1983, *ApJ*, 269, 423
- Shapiro, S. L., Lightman, A. P., & Eardley, D. M. 1976, *ApJ*, 204, 187
- Shimizu, T. T., Meléndez, M., Mushotzky, R. F., et al. 2016, *MNRAS*, 456, 3335
- Stern, B. E., Poutanen, J., Svensson, R., Sikora, M., & Begelman, M. C. 1995, *ApJL*, 449, L13
- Tanimoto, A., Ueda, Y., Odaka, H., et al. 2019, *ApJ*, 877, 95
- Tazaki, F., Ueda, Y., Terashima, Y., & Mushotzky, R. F. 2011, *ApJ*, 738, 70
- Tortosa, A., Bianchi, S., Marinucci, A., et al. 2018a, *MNRAS*, 473, 3104
- Tortosa, A., Bianchi, S., Marinucci, A., Matt, G., & Petrucci, P. O. 2018b, *A&A*, 614, A37

- Tortosa, A., Marinucci, A., Matt, G., et al. 2017, *MNRAS*, **466**, 4193
- Turner, T. J., Reeves, J. N., Braitto, V., & Costa, M. 2018, *MNRAS*, **476**, 1258
- Urry, C. M., & Padovani, P. 1995, *PASP*, **107**, 803
- Ursini, F., Bassani, L., Malizia, A., et al. 2019, *A&A*, **629**, A54
- Ursini, F., Bassani, L., Panessa, F., et al. 2018a, *MNRAS*, **474**, 5684
- Ursini, F., Petrucci, P.-O., Matt, G., et al. 2018b, *MNRAS*, **478**, 2663
- Uttley, P., Cackett, E. M., Fabian, A. C., Kara, E., & Wilkins, D. R. 2014, *A&ARv*, **22**, 72
- Vaiana, G. S., & Rosner, R. 1978, *ARA&A*, **16**, 393
- Vasudevan, R. V., Brandt, W. N., Mushotzky, R. F., et al. 2013, *ApJ*, **763**, 111
- Vasudevan, R. V., Fabian, A. C., Reynolds, C. S., et al. 2016, *MNRAS*, **458**, 2012
- Walton, D. J., Nardini, E., Gallo, L. C., et al. 2019, *MNRAS*, **484**, 2544
- Xu, Y., Baloković, M., Walton, D. J., et al. 2017, *ApJ*, **837**, 21
- Zdziarski, A. A. 1985, *ApJ*, **289**, 514
- Zdziarski, A. A., & Lightman, A. P. 1985, *ApJL*, **294**, L79
- Zdziarski, A. A., Poutanen, J., & Johnson, W. N. 2000, *ApJ*, **542**, 703
- Zhang, J.-X., Wang, J.-X., & Zhu, F.-F. 2018, *ApJ*, **863**, 71
- Zoghbi, A., Matt, G., Miller, J. M., et al. 2017, *ApJ*, **836**, 2